

**UTILIZATION OF ENERGY STORAGE SYSTEMS AND
FACTS DEVICES TO IMPROVE FREQUENCY RESPONSE
IN LOW INERTIA POWER SYSTEMS**

by

Md. Nahid Haque Shazon

(0419062119)

Submitted in partial fulfillment of the requirements of the degree of
Master of Science in Electrical and Electronic Engineering



BANGLADESH UNIVERSITY OF ENGINEERING AND TECHNOLOGY

DHAKA-1000, BANGLADESH

June 2022

**UTILIZATION OF ENERGY STORAGE SYSTEMS AND
FACTS DEVICES TO IMPROVE FREQUENCY RESPONSE
IN LOW INERTIA POWER SYSTEMS**

by

Md. Nahid Haque Shazon

(0419062119)

Submitted in partial fulfillment of the requirements of the degree of
Master of Science in Electrical and Electronic Engineering



Under the supervision of

Dr. Nahid-Al-Masood

Professor

Department of Electrical and Electronic Engineering
Bangladesh University of Engineering and Technology (BUET)

BANGLADESH UNIVERSITY OF ENGINEERING AND TECHNOLOGY

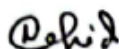
DHAKA-1000, BANGLADESH

June 2022

CERTIFICATION OF THESIS

The thesis titled “**UTILIZATION OF ENERGY STORAGE SYSTEMS AND FACTS DEVICES TO IMPROVE FREQUENCY RESPONSE IN LOW INERTIA POWER SYSTEMS**” submitted by **Md. Nahid Haque Shazon**, Student ID: 0419062119, Session: April, 2019 has been accepted as satisfactory in partial fulfillment of the requirement for the degree of Master of Science (M.Sc.) in Electrical and Electronic Engineering on 14 June 2022.

BOARD OF EXAMINERS



Dr. Nahid-Al-Masood
Professor
Department of Electrical and Electronic Engineering
Bangladesh University of Engineering and Technology, Dhaka,
Bangladesh

Chairman
(Supervisor)



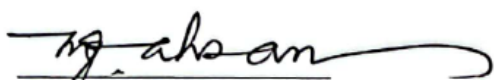
Dr. Md. Kamrul Hasan
Professor & Head
Department of Electrical and Electronic Engineering
Bangladesh University of Engineering and Technology, Dhaka,
Bangladesh

Member
(Ex- officio)



Dr. Abdul Hasib Chowdhury
Professor
Department of Electrical and Electronic Engineering
Bangladesh University of Engineering and Technology, Dhaka,
Bangladesh

Member



Dr. Md. Quamrul Ahsan
Professor
Department of Electrical and Electronic Engineering
Green University of Bangladesh, Dhaka,
Bangladesh

Member
(External)

Candidate's Declaration

I, Md. Nahid Haque Shazon, declare that this thesis titled, "UTILIZATION OF ENERGY STORAGE SYSTEMS AND FACTS DEVICES TO IMPROVE FREQUENCY RESPONSE IN LOW INERTIA POWER SYSTEMS" and the work presented in it are fully my own in partial fulfillment of the requirement for the degree of Master of Science (M.Sc.) in Electrical and Electronic Engineering. I confirm that this research work has not been submitted elsewhere for the award of any degree or diploma excepting for publication. Others' works that have been quoted are clearly attributed with source.

Md. Nahid Haque Shazon

Md. Nahid Haque Shazon

Acknowledgement

All praise goes to the Most Gracious and Most Merciful Almighty ALLAH for enabling me to complete this work.

I would like to express my deepest sense of gratitude to my mentor and supervisor, Dr. Nahid-Al-Masood, Professor, Department of Electrical and Electronic Engineering, Bangladesh University of Engineering and Technology (BUET), Dhaka, for his kind supervision in this work. His undaunted guidance, untiring efforts, great patience, valuable advices and constant assistance extensively helped me to complete this work. He is my not only my supervisor but also a true mentor who will be a significant inspiration to me for rest of my life. Thank you very much Dr. Masood.

Finally, I would like to thank my loving wife, my parents, in-laws and my well-wishers for the support they have provided me with throughout this challenging time.

Abstract

In recent times, due to prolific wind power penetration in many power systems, synchronous generators (SGs) are being substituted from the generation mix worldwide. Unlike the conventional SGs, variable speed Wind Turbine Generators (WTGs) do not participate in frequency regulation without additional control strategy. During prolific wind generation and interconnection import from an adjacent grid, number of online SGs in a network may reduce. In such situation, a large contingency can cause undesirable Rate of Change of Frequency (ROCOF) and frequency deviation. If ROCOF exceeds 2 Hz/s, steam, hydro and wind turbine generators face difficulties to be in synchronism. Furthermore, if ROCOF is higher than 3 Hz/s, the under frequency load shedding relays may fail to respond quickly to shed loads, which can instigate a system-wide blackout. To overcome this problem, deployment of energy storage systems (ESS), namely, Superconducting Magnetic Energy Storage (SMES) and Battery Energy Storage System (BESS) can be a worthwhile solution. This is due to extremely rapid inertial response capability of SMES and ability of BESS to provide active power support for a fairly long duration. Since these devices are costly, their appropriate sizing is crucial. Although numerous sizing schemes of ESS are already investigated in recent literature, none of the existing works deploy and determine the sizes of the ESS separately for providing inertial support and primary frequency response respectively. Furthermore, when the system inertia is insufficient, a large contingency in the power importing zone may overload an AC interconnection. Consequently, the interconnection could trip due to loss of synchronism, which may lead to system-wide blackout. Although series capacitors can be utilized to solve this problem, they demonstrate several drawbacks such as little controllability and risk of sub-synchronous resonance at high compensation levels. Therefore, further investigations are required to meet these research gaps.

In the above perspective, analytical expressions to determine the appropriate sizes of Energy Storage Systems (SMES and BESS) will be formulated in this thesis. Also, a coordinated operational strategy for SMES and BESS to ensure frequency response adequacy will be developed. To avert the risk of cascading contingency and subsequent blackout, a frequency responsive Thyristor Controlled Series Capacitor (TCSC) will be modeled. To this end, optimal TCSC parameters will be determined to ensure minimum frequency deviation. Furthermore, an analytical expression to determine the maximum wind penetration level by

retaining a satisfactory frequency response will be established. Later on, enhancement of maximum wind penetration level after incorporating TCSC will also be estimated.

Table of Contents

Candidate’s Declaration	iv
Acknowledgement	iv
Abstract.....	v
List of Figures.....	x
List of Tables	xii
List of Abbreviations	xiii
List of Symbols	xv
Chapter 1 Introduction.....	1
1.1 Background.....	1
1.2 Motivation.....	3
1.3 Objectives	4
1.4 Outcome of the Thesis	4
1.5 Thesis Organization	5
Chapter 2 Literature Review	6
2.1 Frequency Control Challenges in Low Inertia Grids.....	6
2.2 Existing Frequency Control Strategies	7
2.2.1 Frequency Control Techniques Regarding ESS	7
2.2.2 Techniques for Preventing Network Separation	9
2.2.3 Means for Enhancing Wind Penetration Levels	11
2.3 Research Gaps.....	12
2.4 Summary	13
Chapter 3 Deployment of Energy Storage Systems for Frequency Response Improvement	14
3.1 Grid Frequency Response Characteristics	14

3.2	Frequency Responsive Modeling of SMES	15
3.3	Frequency Responsive Modeling of BESS	17
3.4	Proposed Methodology	18
3.4.1	Sizing of SMES.....	18
3.4.2	Sizing of BESS	20
3.4.3	ESS Scheduling and Energy Rating.....	22
3.4.4	Proposed Strategy for Coordinated Action of ESS.....	23
3.5	Studied Power Grid and Simulation Scenarios	25
3.5.1	Studied Power System	25
3.5.2	Simulation Scenarios	26
3.6	Results and Analyses	27
3.6.1	ESS Ratings	27
3.6.1.1	SMES Size	28
3.6.1.2	BESS Size	28
3.6.2	Improvement of Frequency Response	28
3.6.2.1	Case Study-I.....	29
3.6.2.2	Case Study-II	30
3.6.2.3	Case Study-III	31
3.6.2.4	Case Study-IV	32
3.6.3	Comparison With “Only BESS”	33
3.6.3.1	Case Study-I.....	33
3.6.3.2	Case Study-II	34
3.6.3.3	Case Study-III	35
3.6.3.4	Case Study-IV.....	35
3.7	Further Discussions.....	37
3.7.1	Benefits of The Analytical Approach	37
3.7.2	Applicability of The Proposed Method.....	37
3.7.3	Factors Influencing ESS Response	38
3.8	Summary	39
Chapter 4 Modeling and Utilization of TCSC for Enhancing Frequency Response.....		40
4.1	Frequency Responsive Modeling of TCSC	40

4.2	Proposed Methodology	43
4.2.1	Finding Optimal Parameters of TCSC	43
4.2.2	Enhancement of Wind Penetration Level	45
4.3	Network Overview and Simulation Scenarios	48
4.3.1	Overview of The Low Inertia Grid	48
4.3.2	Simulation Scenarios	50
4.4	Simulation Results and Analyses	50
4.4.1	Optimized TCSC Parameters	50
4.4.2	Frequency Response in High Load Scenario	51
4.4.3	Frequency Response in Low Load Scenario	55
4.4.4	Performance Comparison with An Existing Technique	56
4.4.4.1	100 MW Contingency	56
4.4.4.2	300 MW Contingency	57
4.4.5	Improvement of Maximum Wind Penetration Level	58
4.5	Further Discussions	60
4.6	Summary	61
Chapter 5 Conclusions and Recommendation for Future Research.....		63
5.1	Conclusion	63
5.2	Recommendations for Future Works	64
References.....		66
Appendix A : Test System Data.....		74
Appendix B : List of Publications.....		75

List of Figures

Figure 1.1: Present and targeted renewable penetration levels by countries	1
Figure 1.2: Growth of global installed wind generation capacity.....	2
Figure 3.1: Stages of power system frequency response	15
Figure 3.2: General configuration of a CSC-based SMES.....	16
Figure 3.3: (a) Active power control block of CSC-based SMES (b) ROCOF sensitive auxiliary signal model.	17
Figure 3.4: Energy control strategy of BESS.....	17
Figure 3.5: Proposed strategy for coordinated operation of SMES and BESS.....	24
Figure 3.6: Single-line diagram of simulated power system	26
Figure 3.7: (a) Frequency response in case study - I (b) SMES output in case study - I (c) BESS output in case study – I.....	30
Figure 3.8: (a) Frequency response in case study- II (b) SMES output in case study- II (c) BESS output in case study –II	31
Figure 3.9: Frequency response in case study- III.	32
Figure 3.10: Frequency response in case study- IV	33
Figure 3.11: Frequency response in case study- I.....	34
Figure 3.12: Frequency response in case study- II..	34
Figure 3.13: Frequency response in case study- III.....	35
Figure 3.14: Frequency response in case study- IV	36
Figure 4.1: Basic configuration of TCSC.	40
Figure 4.2: Block diagram of a frequency responsive TCSC	42
Figure 4.3: Flowchart to obtain optimised TCSC parameters	45
Figure 4.4: Relationship between frequency nadir and WPL	48
Figure 4.5: Network diagram of the simulated system.....	50
Figure 4.6: System performance for 5 machines case in high load scenario.....	53
Figure 4.7: Frequency response of Area-3 for 5 machines case in high load scenario.....	54
Figure 4.8: System performance for 4 machines case and 3 machines case in high load scenario	55
Figure 4.9: Frequency response for low load scenario	56
Figure 4.10: Frequency response comparison with existing technique for 100 MW contingency	57

Figure 4.11: Frequency response comparison with existing technique for 300 MW contingency58

Figure 4.12: Maximum WPL without and with TCSC in 5 machines case (a) High load scenario
(b) Low load scenario.....59

List of Tables

Table 3.1: Conventional powerplant information	25
Table 3.2: Simulation scenarios	27
Table 3.3: Summary of the simulation results	36
Table 3.4: Summary of the load shedding amounts	37
Table 4.1: Conventional power plant information	49
Table 4.2: Simulation scenarios	51
Table 4.3: Optimised TCSC parameters	52
Table 4.4: Enhancement in Maximum WPL	60

List of Abbreviations

RES	Renewable Energy Sources
DFIG	Doubly-Fed Induction Generator
WTGs	Wind Turbine Generators
HVAC	High voltage AC
HVDC	High voltage DC
DGs	Distributed Generators
ESS	Energy Storage Systems
SMES	Superconducting Magnetic Energy Storage
BESS	Battery Energy Storage System
TCSC	Thyristor Controlled Series Capacitor
ROCOF	Rate of Change of Frequency
UFLS	Under Frequency Load Shedding
DESS	Dynamic Energy Storage System
SCES	Supercapacitor Energy Storage
FSC	Fixed Series Capacitors
FESS	Flywheel Energy Storage System
FACTS	Flexible AC Transmission Systems
PSS®E	Power System Simulator for Engineering
GA	Genetic Algorithm
DR	Demand Response
SSSC	Static Synchronous Series Compensators
WPL	Wind penetration level
WTG	Wind turbine generator
PFR	Primary Frequency Response
IR	Inertial response
SFR	Secondary frequency response
TFR	Tertiary frequency response
EPRI	Electric Power Research Institute
CSC	Current Source Converter
p.u.	Per unit
VSC	Voltage-Source Converter

SoC	State of Charge
TSO	Transmission System Operator
PSO	Particle Swarm Optimization
LFR	Load Frequency Relief
SSR	Sub-Synchronous Resonance

List of Symbols

P_{init}	Initial active power of the SMES
I_{DC0}	Initial DC current
I_{DC}	Coil DC current
V_{DC}	Coil DC voltage
P_{DC}	DC input power
K_R	DC current gain
P_{MAX}	Rated power of SMES
I_{DCMIN}	Coil current lowest limit
I_{DCMAX}	Coil current highest limit
I_{ACMAX}	Converter current limit
P_{AUX}	Auxiliary power signal
E_{rated}	Rated energy of SMES
T	Maximum time duration for delivering power by SMES
I	Maximum coil current of SMES
L	SMES coil inductance
E_{OUT}	The amount of energy absorbed or supplied by the BESS
OUT_{EFF}	Retrieval efficiency of BESS
INP_{EFF}	Storage efficiency of BESS
E_{rated}	Rated energy of SMES
R_{max}	Magnitude of maximum allowable ROCOF limit
f_o	Nominal system frequency
IR	System inertia
ΔP_g	Change in generation
ΔP_L	Change in system load
S_i	Rated MVA of $i - th$ synchronous generator
H_i	Inertia constant of $i - th$ synchronous generator
$SMES_{size}$	Required rated size of SMES
P_L	System load including loss
$BESS_{size}$	Required rated size of BESS
k_p	Load frequency relief

f_{min}	Predefined threshold frequency
R	Droop
T_s	System equivalent time constant
ϕ	Frequency deviation following a contingency
SoC_{min}	Minimum SoC limits
SoC_{max}	Maximum SoC limits
SoC_t	SoC at any instant
SoC_0	Initial State of Charge
$P_{BESS,t}^{ch}$	Instantaneous amount of charge of BESS
$P_{BESS,t}^{dch}$	Instantaneous amount of discharge of BESS
$P_{SMES,t}^{ch}$	Instantaneous amount of charge of SMES
$P_{SMES,t}^{dch}$	Instantaneous amount of discharge of SMES
P_{BESS}^{chmax}	Charging limits of BESS
P_{SMES}^{chmax}	Charging limits of SMES
P_{BESS}^{dchmax}	Discharging limits of BESS
P_{SMES}^{dchmax}	Discharging limits of SMES
ESS_{size}	Rated size of ESS
V_1	The receiving end voltage magnitude
V_2	The sending end voltage magnitude
δ_1	The receiving end voltage angle
δ_2	The sending end voltage angle
X_L	Inductive reactance of TCSC
X_C	Capacitive reactance of TCSC
X_{Line}	The total reactance of the tie-line without TCSC
X_{TCSC}	The total reactance of TCSC
ΔP_{tie}	Total change in tie-line flow
k_c	Composition factor of TCSC
ΔP_{tie}^0	Change in initial tie-line flow
ΔP_{TCSC}	Change in tie-line flow due to TCSC installation
$\Delta \alpha$	Change in firing angle
$\Delta \omega$	Speed deviation following a contingency
x	Final reactance of the tie-line

T_1, T_2, T_3	Time constants of TCSC block
k	Gain of the TCSC block
v_{id}	The velocity of the $i - th$ particle
P_{id}	The position of $i - th$ particle in a d dimensional space for $m-th$ iteration
$Pbest_i$	The previous best position
$Gbest$	Global best of the swarm
acc_1, acc_2	Acceleration constant of the particles
$rand_1, rand_2$	Random numbers having a value between 0 to 1
$\Delta f(t, X)$	The maximum amount of deviation from the nominal frequency
OF	Objective function
$T_2^{min}, T_3^{min}, k_{min}$	Minimum allowable values of the corresponding variables
$T_2^{max}, T_3^{max}, k_{max}$	Maximum allowable values of the corresponding variables
P_{wind}	The total wind power
P_{sync}	The total synchronous generation
P_{import}	The total interconnection import
f_{TH1}	Frequency threshold to activate the 1st stage of load shedding
f_{TH2}	Frequency threshold to activate the 2ndstage of load shedding
f_{TH3}	Frequency threshold to activate the 3rd stage of load shedding
m_1, m_2, m_3	Percent of load is shed in three stages

Chapter 1

Introduction

1.1 Background

Owing to the detrimental effects on the environment and limited accessibility of fossil fuels, a global trend of reliance on Renewable Energy Sources (RES) has emerged. Note that coal-based power plants are one of the most common sources of greenhouse gases [1]. Unlike these conventional fossil fuel driven generators, RES can offer green energy, which can be instrumental for abating the harmful effects of fossil fuels. Moreover, it can satisfy the burgeoning global power demand. It is anticipated that within next 30 year, the Denmark power system will be able to reach 100% RES penetration landmark [2]. The European union, United States and China have also set definite targets for RES integration in respective power systems [3]. Current renewable penetration levels and future targets of several countries are articulated in Figure 1.1. It shows that Ireland, China, Spain, India and Europe intend to include more than 90% renewable resources in their power systems within 2050 [4].

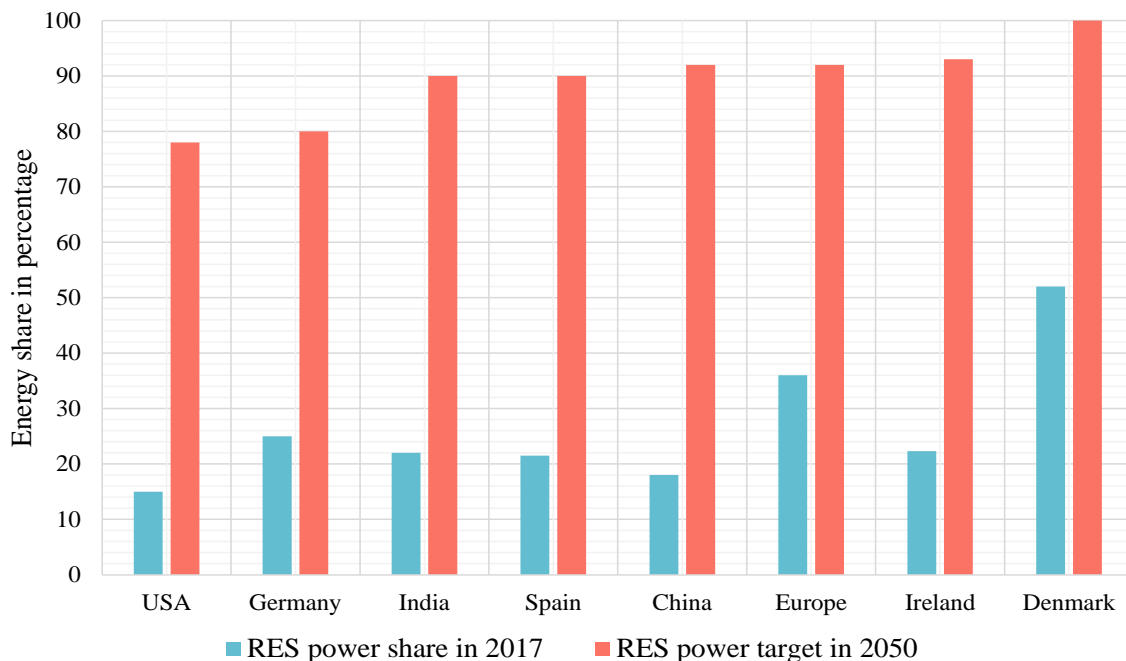


Figure 1.1: Present and targeted renewable penetration levels by countries.

Various RES- solar, wind, biomass, hydro, geothermal, ocean power etc. are being tried out by system operators around the world to fulfil the energy requirements set by respective regulatory bodies. Among them, wind power plants (especially Doubly Fed Induction

Generators: DFIG) have been one of the most promising one [5]. The total installed capacity for onshore and offshore wind energy globally is over 651 GW by the end of 2019 [6]. The proliferation of wind power generation capacity around the world in the last decade is shown in Figure 1.2.

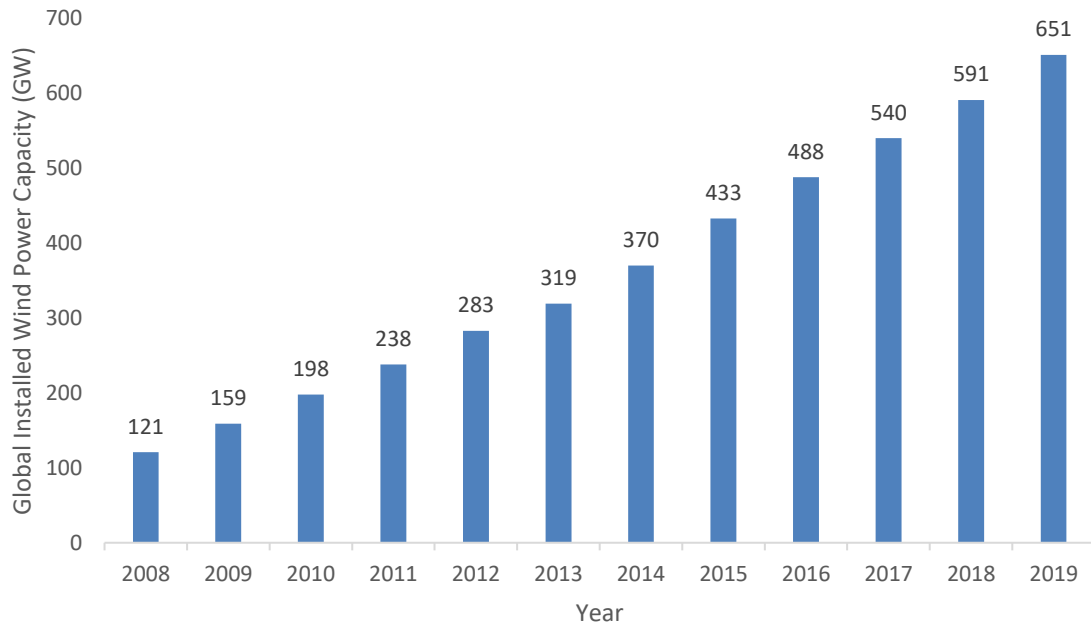


Figure 1.2: Growth of global installed wind generation capacity [6].

Note that a wind energy conversion system converts the kinetic energy of wind into electricity by using a large wind turbine which consists of blades on a shaft. Since the shaft of the turbine is connected to a generator, the rotating motion of the shaft rotates the generator's rotor. Consequently, an electromagnetic induction is created due to the rotational movement of the rotor inside the generator core, which ultimately produces electrical power.

Wind turbine generators (WTGs) can be divided into four main types: Type 1 (Fixed Speed Induction Generator), Type 2 (Variable-Slip Induction Generator), Type 3 (Doubly-Fed Induction Generator: DFIG) and Type 4 (Full-Scale Converter) machines [7]. A squirrel-cage induction generator is used in a Type 1 WTG. Whereas a wound-rotor induction generator is deployed in Type 2 WTG [3]. A Type 3 WTG is a variable speed machine where an induction generator and power electronic converters are utilized. In a Type 4 WTG, the generator can be an induction generator or a synchronous generator. It is worthwhile to mention that the generator is connected to the grid via power electronic converters [7].

It must be noted that wind power plants suffer from the unprecedented disadvantage of intermittency or fluctuation. As a result, power system operators have to be concerned about variable generation as well as uncontrollable demand in future power systems. In addition, both

Type 3 and Type 4 wind generators are connected with the host power grid via power electronic converters. In case of conventional fossil fuel driven synchronous generators, their rotors are directly connected with the host grid and behave as spinning reserves. These spinning reserves can absorb or supply the stored kinetic energy in case of a power deficit or surplus [8]. This stored kinetic energy acts as inertia of the rotors and is an inherent property of conventional generators. As Type 3, 4 wind generators are decoupled from the host power systems, they do not necessarily contribute to system inertia without additional control mechanisms [9]. This system inertia could have arrested the change in speed of generator rotors (equivalent to system frequency).

1.2 Motivation

As discussed above, wind-dominated power systems may suffer from inadequate system inertia due to retirement of conventional fossil-fuel driven synchronous generators. Furthermore, a load-rich area can import electricity from an adjacent generation-rich area through a high-voltage AC (HVAC) or high-voltage DC (HVDC) line in modern interconnected power systems. As a result, the number of conventional generators in a load-rich region can be minimal. Loss of this interconnection can cause a major power imbalance and substantial deviation from nominal system frequency. Thus, frequency decline in a low inertia system can lead to cascaded trip, which can even lead to system-wide blackout. To mitigate these issues, deployment of energy storage systems (ESS), namely, Superconducting Magnetic Energy Storage (SMES) and Battery Energy Storage System (BESS) can be a worthwhile solution due to the extremely rapid inertial response capability of SMES and ability of BESS to provide active power support for a fairly long duration. This strategy can be regarded as frequency control from load perspective. Since these devices are costly, their appropriate sizing is crucial. Although numerous sizing schemes of ESS are already investigated in recent literature, none of the existing works deploy and determine the sizes of the ESS separately for providing inertial support and primary frequency response respectively. Furthermore, when the system inertia is insufficient, a large contingency in the power importing zone may overload an AC interconnection. Consequently, the interconnection could trip due to loss of synchronism, which may lead to system-wide blackout. Although series capacitors can be utilized to solve this problem, which is a frequency control strategy from generation perspective, they demonstrate several drawbacks such as little controllability and

risk of sub-synchronous resonance at high compensation levels. Therefore, further investigations are required to meet these research gaps.

1.3 Objectives

The principal goal of this thesis is to enhance the system frequency response of a low inertia grid by the utilization of Energy Storage Systems and frequency responsive Thyristor Controlled Series Capacitor (TCSC). The specific objectives of this work are as follows:

- i. To formulate analytical expressions to determine the appropriate sizes of Energy Storage Systems (SMES and BESS). SMES rating will be determined using ROCOF limit due to its dominant participation during inertial response, and BESS rating will be decided by the allowable frequency deviation due to its major participation during primary frequency response.
- ii. To develop a coordinated operational strategy for SMES and BESS to ensure frequency response adequacy.
- iii. To model a frequency responsive Thyristor Controlled Series Capacitor (TCSC) to avert the risk of cascading contingency and subsequent blackout. To this end, optimal TCSC parameters are to be determined to ensure minimum frequency deviation.
- iv. To establish an analytical expression to determine the maximum wind penetration level by retaining a satisfactory frequency response. Later on, enhancement of maximum wind penetration level after incorporating TCSC will also be estimated.

1.4 Outcome of the Thesis

The outcome of this thesis will provide the appropriate sizes of SEMS and BESS while retaining satisfactory frequency deviation and Rate of Change of Frequency (ROCOF). Also, the outcome will yield a frequency responsive TCSC model for preventing network separation and system-wide blackout. In addition, the thesis will provide an analytical formulation of the maximum wind penetration level for ensuring adequate frequency response. Therefore, the

outcome of this thesis work will help enabling large-scale integration of renewable generation and provide useful guidelines for system operators to improve frequency resilience.

1.5 Thesis Organization

This thesis consists of five chapters. The structure of the thesis is as follows:

- In chapter 1, a brief description of current and future global wind energy scenario is described. Then, motivation of the current work is presented along with the objectives.
- In chapter 2, a thorough review of relevant recent works is narrated. Later on, the research gaps are identified.
- In chapter 3, at first, the frequency responding modeling of SMES and BESS are discussed. Afterwards, analytical methodologies for determining the SMES and BESS size is established. Afterwards, a coordinated operational strategy for SMES and BESS to ensure frequency response adequacy is developed. Then, several simulation scenarios are formed to test the effectiveness of the proposed ESS sizing method. Afterwards, those scenarios are investigated by using a test low inertia power system to validate the proposed strategies.
- In chapter 4, at first, a frequency responsive Thyristor Controlled Series Capacitor (TCSC) to avert the risk of cascading contingency and subsequent blackout is modeled. To this end, optimal TCSC parameters are determined to ensure minimum frequency deviation. Several simulation scenarios are investigated to prove the effectiveness of the abovementioned method. In addition, an analytical expression to determine the maximum wind penetration level is established. Later on, enhancement of maximum wind penetration level after incorporating TCSC is estimated.
- Finally, in chapter 5, the key findings are summarized and the possibilities of future research work are mentioned.

Chapter 2

Literature Review

In this chapter, firstly, the major frequency control challenges caused by higher wind power penetration are shortly described. Then, a comprehensive literature review on frequency control strategies and means for enhancing wind penetration levels are presented. Finally, research gaps are identified.

2.1 Frequency Control Challenges in Low Inertia Grids

In recent times, increased integration of wind power plants have introduced several challenges regarding the frequency response adequacy, especially in low inertia power systems. The reason behind this is, as discussed in the previous section, nowadays wind power plants predominantly utilize Type 3 (Doubly Fed Induction Generator: DFIG) and Type 4 (Full-Scale Converter) machines. These variable speed machines are isolated from the grid through power electronic converters [10]. Therefore, they generally do not provide inertia and governor response (also known as primary frequency response) unless additional control strategy is implemented [11]. As such, frequency response after a major contingency is likely to become more vulnerable under high wind power penetration [12]. Situations can arise where a system has substantial wind penetration while it imports bulk amount of power through high voltage AC (HVAC) interconnection from adjacent grid. During this situation, a large contingency (e.g. tripping of an interconnection) may cause unacceptable frequency excursion with a high Rate of Change of Frequency (ROCOF) and frequency deviation. Consequently, significant Under Frequency Load Shedding (UFLS) may need to be applied to arrest the frequency decline.

Note that when ROCOF exceeds 2 Hz/s, steam, hydro and wind turbine generators face difficulties to be in synchronism [13]. Furthermore, if ROCOF is higher than 3 Hz/s, the UFLS relays may fail to respond quickly enough to shed necessary amount of loads. It eventually could result in a system wide blackout [14]. Furthermore, while shedding loads, distributed generators can also get disconnected [15]. Such incident makes frequency response even worse, which ultimately leads to further load shedding. Therefore, necessary techniques need to be adopted to avoid high ROCOF and large frequency deviation to improve the frequency resilience of low inertia power grids.

Moreover, the number of committed SGs can be scant when wind power generation is substantial in quantity and the system is importing power through high voltage AC (HVAC)

interconnection from an adjacent area. Accordingly, system inertia of that particular zone and governor responsive reserve for that area are considerably reduced. In such a situation, the system intends to draw more power via the HVAC interconnection following a contingency (For instance, a large generator trip). However, if the interconnection flow reaches the maximum limit, it incurs loss of synchronism. As a result, the interconnection trips, which can cause a cascading contingency for the power importing region. In this situation, the isolated network may encounter a blackout if the primary frequency control and the UFLS mechanism fail to stop the frequency decline. For instance, South Australia encountered a similar blackout in 2016, which was initiated by the loss of HVAC interconnection between South Australia and Victoria [14]. Therefore, necessary techniques need to be developed to prevent network separation and subsequent blackout in low inertia power systems under high wind penetration. Note that the adverse effects on modern grids created by the proliferation of renewable resources are preventing further integration of intermittent yet environment friendly energy resources. Therefore, additional regulation services need to be employed to continue the current trend of burgeoning renewable penetration.

2.2 Existing Frequency Control Strategies

Extensive research is conducted to address the frequency control issues depicted in the previous subsection. This subsection intends to outline the recent studies regarding emulated inertia from energy storage systems for maintaining satisfactory frequency response with a tolerable ROCOF and frequency deviation. In addition, means for preventing network separation and subsequent cascaded contingency are also discussed. Furthermore, recent research works regarding techniques of enhancing wind and other renewable penetrations are depicted.

2.2.1 Frequency Control Techniques Regarding ESS

Various strategies are explored in the existing literature to improve the frequency response of low inertia grids via load perspective using various storage technologies, for instance, synthetic inertia and governor like response from energy storage systems. For example, utilization of synchronous condensers is reported in [16], which can provide supplementary inertial response. Furthermore, synchronous condenser and synthetic inertia from wind power plants are jointly used in [17] to enhance frequency stability. Note that in both of these works, the ratings of synchronous condensers are chosen based on corresponding

simulated grid topology. Thus, no analytical methodology is developed to find the optimal size of additional frequency support device (i.e., synchronous condensers).

A methodology is developed in [18] to incorporate virtual inertia support from wind plants into generation scheduling by utilizing the DC-link inertia control, the VCC strategy and power-frequency droop control. However, neither the competence of the proposed methodology is compared with any existing technology nor value proposition of the proposed methodology is illustrated in this work. Furthermore, various storage technologies are utilized for achieving fast frequency response [19]. Among them, Li-ion batteries are widely used as storage medium. Alternative lithium batteries [20], Ni-Cd, lead-acid, vanadium redox flow batteries, flywheels [21], Supercapacitor Energy Storage (SCES) [22] and Superconducting Magnetic Energy Storage (SMES) [23] are also employed for frequency support. Their response time, installation cost, operational cost, sustainability and life spans are described in [24]. However, none of these illustrated works emphasis on finding appropriate sizing of the aforementioned energy storages along with frequency response adequacy. For instance, in [22], the authors only demonstrate the competence of ultracapacitor installation under different load condition. Furthermore, effectiveness of supercapacitor installation is not compared with any existing technologies such as synchronous condenser, BESS, SMES and so on. In [25], ultracapacitor storage is used as a Dynamic Energy Storage System (DESS) to offer emulated inertial support. Nevertheless, the authors primarily focus on structure and control of the DESS instead of its sizing. In [26], an optimally sized Battery Energy Storage System (BESS) is incorporated to provide primary frequency response, where BESS size is determined solely based on economic aspect without taking frequency response adequacy in different conditions into account.

In [27], a bi-level optimization model is developed for achieving maximum profit where the model is converted into a mixed-integer linear program. According to this algorithm, the optimal size of the energy storage depends on system fault condition, duration of load curtailment under various fault scenarios and enhancement of profitability in terms of unit income for distribution system. However, system resilience is neither investigated under altering renewable penetration level nor system operating conditions such as frequency and ROCOF are taken into account.

In [28], authors propose a sizing scheme for energy storage systems to mitigate significant changes in power outputs of intermittent sources. The authors consider generator ramp-rate limits, the efficacy of storage system (State of Charge limits) and optimal dispatch of the energy storage systems along with curtailment of intermittent resources. The primary

objective of this work is to obtain an optimal energy storage size so that minimum curtailment of renewable sources is achieved. Nevertheless, the sizing strategy does not take any other system operating conditions into consideration and implementation of this algorithm does not depend on any system parameters. In addition, there is no indication that which storage device would be preferable to obtain maximum profitability.

The authors propose a sizing scheme for Battery Energy Storages, which solely depends on optimizing operational cost of a microgrid and minimizing BESS charging and discharging capacity in [29]. This research work investigates the competence of the proposed method in three different scenarios depending on whether the microgrid is connected with the host grid and power can be sold to the host grid. Thus, system performance is not examined in terms of allowable frequency deviation and system ROCOF limits.

In [30], authors incorporated a multi-objective grey wolf optimizer to determine optimal Hybrid Energy Storage System size considering system operating cost and battery lifespan. Competence of the methodology has been scrutinized by comparing the obtained total energy loss with that of RF based Energy Management System. In [31], authors propose a sizing methodology of ESS to determine ESS rated power and energy capacity for providing inertial and primary frequency support by utilizing linearized swing equation.

2.2.2 Techniques for Preventing Network Separation

To prevent network separation following a generation deficit in a load rich area, energy storage techniques can be utilized since they can provide fast frequency response [32, 33]. For instance, in [34], the authors proposed the utilization of hybrid energy storage system consisting of BESS and SCES, which is able to enhance the load frequency controllability of an interconnected system. This work mainly focuses on suppressing frequency deviation and tie-line flow fluctuations caused by load variability. Several recent works have suggested demand response strategies for renewable dominated power systems [35, 36]. In [35], the authors propose a fuzzy cascade controller with demand response, which has the capability of load disturbance rejection in an interconnected microgrid. The authors of [36] claim and justify that improving demand response is an efficient way of optimizing power imbalance in electric grids. Note that the above methods enhance frequency response of individual power systems. However, these approaches do not assure the prevention of network separation, especially for low inertia grids. In [37] and [38] the authors focus on quantifying the required zonal inertia to obtain satisfactory frequency response following network separation. Notably the zonal inertia

may be able to restrict the system ROCOF following the contingency. However, it may not guarantee the prevention of network separation and subsequent blackout.

For preventing network separation, the power carrying capability of an interconnection needs to be increased. Providing series compensation can lower overall reactance of an interconnection and enhance power carrying capability of that line, which is a frequency control technique from generation perspective. For this purpose, mechanical switch controlled Fixed Series Capacitors (FSC) has been the traditional choice for years. However, they demonstrate several drawbacks that are summarized below [39]:

- At higher compensation level (more than 50%), they lack effective controllability.
- They do not offer smooth controllability when compensation levels are being altered.
- While altering compensation levels, re-inserting capacitors may result in undesirable voltage offset across it.
- At high compensation levels, risks of sub-synchronous resonance increase, especially in presence of variable speed WTGs. Additional damping circuit will be required in such situations, which will increase network complexity and cost.

Following the progress of power electronic devices and switching technology, Flexible AC Transmission Systems (FACTS) devices are deployed to increase the power transfer limits of interconnections. For instance, TCSC, which is a FACTS device, can be utilized to decrease the reactance of an AC transmission line [40]. As such, power carrying capacity of that line increases. Notably, TCSC has the ability to overcome all the drawbacks of FSC and have the capability to offer much more reliable system performance. In addition, TCSC can provide other benefits. These include damping of small signal oscillation [41], compensation of transmission line while minimizing the sub-synchronous resonance [42], frequency stabilization of interconnected power systems [43] and enhancement of transient stability [44]. In [45], Thyristor Controlled Series Capacitor (TCSC) is deployed for load following purpose in a two-area interconnected system with the objective of reducing inter area tie-line power error. Optimal parameters in this study are determined by Genetic Algorithm (GA) with the target of obtaining power exchange and area frequencies with the least overshoot and minimized settling time. However, this study does not concentrate on preventing network separation. In addition, although integral gains of TCSC model are optimally tuned in this paper, they are not tuned to yield minimum frequency deviation following a contingency.

2.2.3 Means for Enhancing Wind Penetration Levels

For enhancing wind and other renewable penetrations in modern grids, several means are reported in the literature. Energy storages are considered to be one of the most promising measures in this regard. To this end, authors in [46] suggest the utilization of Flywheel Energy Storage System (FESS) to provide spinning reserve in an isolated power grid. The results demonstrate that FESS installation results in increased system stability and enhanced the renewable penetration of the studied grid. Pumped storages are suggested to enhance wind penetration levels in autonomous islanded grids in [47]. In this study, operating policies and strategies are discussed for wind-hydro-pumped-storage hybrid stations with the target of enhancing wind penetration. In [48], novel strategies for Demand Response (DR) is employed for mitigating operational uncertainties of wind generation. In order to accomplish that, loads are classified in three categories- loads having virtual energy storage capabilities, loads having load shifting capabilities and loads having curtailment capability. However, with the increase of contingency size, the required sizes of energy storages increase. As a result, associated capital and operational costs increase. Authors in [49] introduce the utilization of FACTS devices for enhancing the penetration of wind and solar power. Due to their capability of delivering fast active and reactive power, this paper recommends deploying FACTS devices for mitigating power quality problems which are associated with intermittent wind and solar plants. However, in this work, FACTS devices are not incorporated with the objective of increasing wind penetration while maintaining the system frequency above preset threshold. Rather they focus on mitigating voltage swell, voltage sag, flickers, harmonics and electrical behaviors of switching operations. In [50], the authors demonstrate by load flow analysis that utilization of Static Synchronous Series Compensators (SSSC) can enhance power carrying capabilities of lines and accommodate enhanced renewable penetration. However, neither any analytical framework is proposed to quantify the amount of renewable penetration enhancement, nor any dynamic simulation is shown to bolster their claim. Also, no comparison with existing technology is demonstrated for enhancing power carrying capabilities of the interconnections. In [51], the author utilized SSSC for controlling the power flow through a transmission line in order to mitigate Ferranti effect on unloaded lines. Thus, this study mainly focuses on mitigating power quality issues, such as oscillation damping by dynamic control of FACTS devices.

2.3 Research Gaps

From the literature review regarding frequency control techniques related to ESS, the limitations of these research works are summarized below.

- Some of the existing works do not concurrently consider frequency deviation, system ROCOF, inertial response and governor response for determining the ratings and competence of ESS.
- Over-dependency on time-domain simulations and optimization algorithms is noticed, which consider only profit maximization and battery state of charge to determine ESS sizes.
- Linearization of swing equation is done in many existing works to find optimal ratings of ESS. Consequently, the dynamic attributes of frequency excursion is not fully captured.
- Limited analyses of value proposition of ESS considering their installation, operation and maintenance costs are reported.

Lately, SMES has attracted the attention of researchers for its enormous charge/discharge cycles, rapid response time and high peak current handling capabilities [52]. Generally, SMES is utilized for providing short time storage support. In contrast, BESS is usually installed to deliver storage support for longer period. Consequently, combination of SMES and BESS is taken into account in various applications. These include compensating load variations in railway systems [53], mitigation of wind intermittency [52], electric vehicle operation [54] and so on.

It is evident that SMES can be used for providing additional inertial response to limit ROCOF. In addition, BESS can be used for offering inertia support as well as primary frequency response (i.e., akin to governor response) to arrest the frequency excursion above a certain threshold. Therefore, a combination of SMES and BESS can be beneficial to reinforce the frequency resilience of a low inertia grid. However, coordinated action of SMES and BESS to improve frequency response of renewables dominated power systems remains unresolved in the recent literature. Note that SMES and BESS are costly devices. Hence, their appropriate sizing and operational approach are crucial. Yet, the existing works lack the analytical determination of the sizes of these storage devices in perspective of frequency response adequacy.

Furthermore, from the literature review regarding network separation prevention, it is evident that TCSC has numerous applications in power system. However, the existing works

have not implemented a frequency responsive TCSC model to reduce frequency deviation and blackout mitigation in an interconnected low inertia grid. Even though FSC can be utilized to solve this issue, it comes with numerous disadvantages as depicted in subsection 2.2.2. In addition, no recent literature that the candidate is aware of illustrates system performance comparison between FSC and TCSC in preventing network separation. Also, the maximum wind penetration level is likely to increase when TCSC is deployed to enhance the power carrying capability of the interconnection. Nevertheless, no recent study elaborates on the deployment of TCSC in that regard while developing any analytical framework.

Therefore, further investigations are still required to meet these important yet unaddressed research gaps.

2.4 Summary

In this chapter, a comprehensive insight into the frequency response challenges associated with the prolific wind penetration in power systems is presented. Notably, extensive research has been conducted regarding frequency response improvement strategies. Subsequently, frequency control techniques regarding energy storage systems and means for preventing network separation are discussed in this chapter. Afterwards, drawbacks of the existing literature is outlined and research gaps are depicted. In the above context, in the upcoming chapters, an analytical tool to determine the minimum ratings of ESS is proposed along with a coordinated operational strategy for SMES and BESS to ensure frequency response adequacy. Afterwards, a frequency responsive TCSC to avert the risk of network separation and subsequent cascading contingency is modeled in this thesis. To this end, optimal TCSC parameters are determined to ensure minimum frequency deviation. In addition, an analytical expression to determine the maximum wind penetration level is established. Later on, enhancement of maximum wind penetration level after incorporating TCSC is estimated.

In the following chapters of this thesis, necessary theoretical background, developed methodologies and relevant investigations are thoroughly presented.

Chapter 3

Deployment of Energy Storage Systems for Frequency Response Improvement

In this chapter, firstly, a brief insight into grid frequency response characteristics is outlined. Later on, frequency responsive SMES and BESS models are discussed. Subsequently, the proposed methodology is outlined. Afterwards, simulation scenarios are formed and investigated accordingly to prove the competence of the proposed method.

3.1 Grid Frequency Response Characteristics

Following an imbalance between load and generation, system frequency exhibits different stages. Just after a contingency, stored kinetic energy from the rotors of synchronous generators is inherently released. This is known as inertial response (IR). Duration of this stage is very low- typically within first few seconds after a contingency. The next stage is primary frequency response (PFR). In this stage, generators increase their output according to their droop characteristics and headroom (i.e. governor responsive reserve) for stabilizing the system frequency. IR and PFR persist for around 10 – 30 s from the contingency [55]. Quantity and duration of IR and PFR affect the ROCOF (i.e. df/dt) and frequency nadir. Subsequently, secondary frequency response (SFR) comes in action and PFR is relieved. SFR persist for around 15 minutes and can be controlled both automatically and manually. Finally, tertiary frequency response (TFR) brings back the system frequency to its nominal value by re-dispatching the generators. Figure 3.1 demonstrates the above-mentioned stages with necessary annotations.

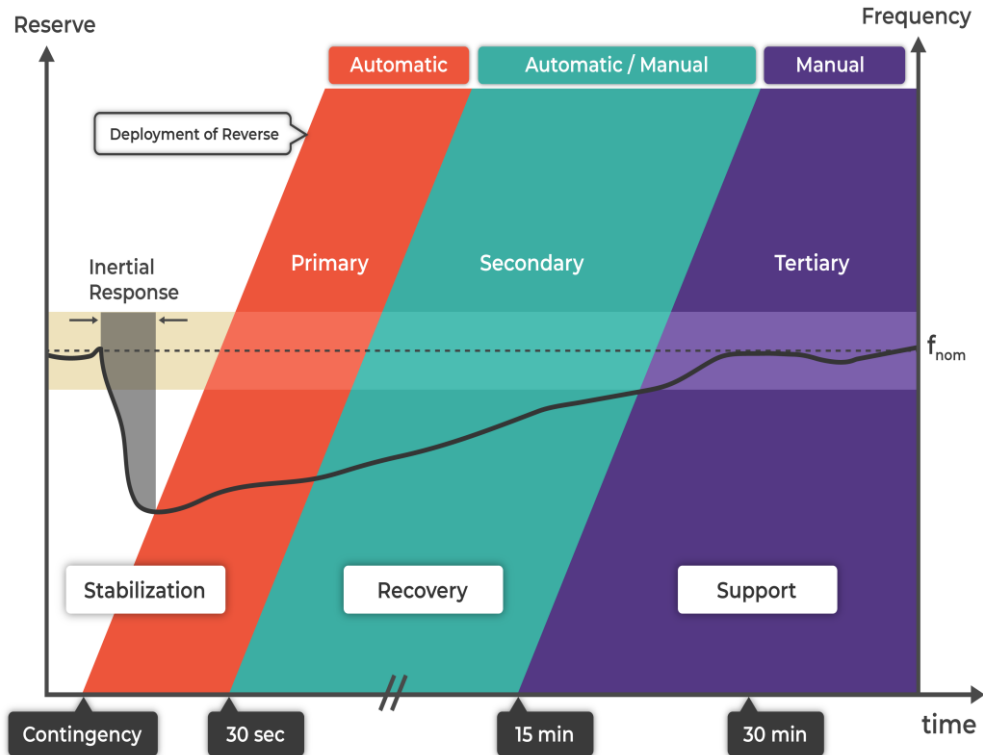


Figure 3.1: Stages of power system frequency response

3.2 Frequency Responsive Modeling of SMES

Electric Power Research Institute (EPRI) CSMEST model is considered in this thesis for SMES modeling [56]. Here, SMES is modelled via a Current Source Converter (CSC). AC side of SMES is linked to the grid, whereas the DC side is directly connected to superconducting coil. A general configuration of CSC-based SMES is demonstrated in Figure 3.2. Here, the capacitors are deployed for buffering the stored energy in line inductances while commuting the direction of grid current. In addition, these capacitors have the capability of filtering out higher order harmonics of the grid current. Fast transfer of active power between SMES and the grid is viable as the modelled SMES in this paper uses CSC. Eventually, it enables SMES to provide emulated inertial response following a contingency.

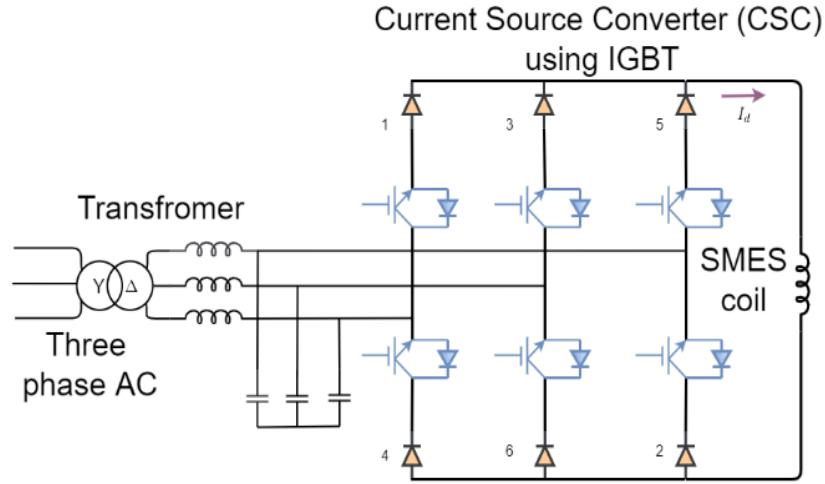


Figure 3.2: General configuration of a CSC-based SMES

Active power control block of SMES is portrayed in Figure 3.3(a). In Figure 3.3(a), P_{init} denotes the initial active power of the SMES (in p.u.), I_{DC0} is the initial DC current (in p.u.), I_{DC} refers to the coil DC current (in p.u.), V_{DC} is the coil DC voltage (in p.u.) that depends on coil DC input power P_{DC} (in p.u.), K_R denotes DC current gain and P_{MAX} is the rated power (in p.u.). It is also equal to the minimum current (in p.u.) at which rated power can be delivered (when the maximum DC voltage applied to the coil terminal is 1 p.u.). Maximum voltage capability of the coil and converter is controlled by V_{DCMAX} and V_{DCMIN} (in p.u.) [56]. Note that I_{DC} is an independent variable and V_{DC} is a function of I_{DC} . I_{DCMIN} and I_{DCMAX} are the coil current limits, which prevent the coil overcharging or undercharging. For the upper saturation limit, the value of I_{DC} should be a subset of I_{DCMIN1} . For the lower saturation limit, the chosen value of I_{DC} should be a superset of I_{DCMAX1} .

In this block, converter current limit is modeled by I_{ACMAX} (in p.u.). Lower limit of current coil of CSC is indicated by $KV_{AC}I_{DC}$, where V_{AC} is the grid AC voltage (in p.u.) and K is a constant gain. Also, $MBASE$ (in p.u.) is calculated by maximum coil voltage times maximum coil current. The value of SMES coil inductance L (in H) can be derived using power and energy rating of the SMES. Rated energy E_{rated} is calculated using (1) and the corresponding inductance can be derived using (2) [56].

$$E_{rated} = P_{MAX}T \quad (1)$$

$$\frac{1}{2}L(I^2 - P_{MAX}^2) = P_{MAX}T \quad (2)$$

where T is defined as maximum time duration for delivering power (in s) and I is the maximum coil current (in p.u.).

Input of the active power block is P_{AUX} , which is a ROCOF sensitive auxiliary power signal. This auxiliary signal block is shown in Figure 3.3(b). It comprises low pass filter, time delay block, constant gain and max-min limiter block. Therefore, when ROCOF exceeds a preset threshold, this block generates an auxiliary power signal. This auxiliary power signal changes (increase/ decrease) the active power output of SMES.

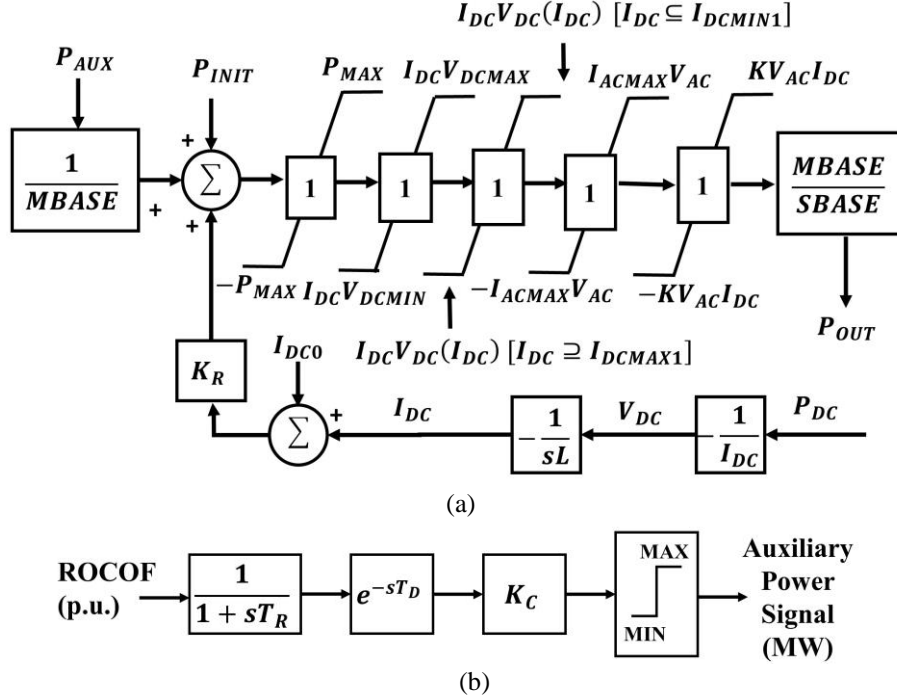


Figure 3.3: (a) Active power control block of CSC-based SMES (b) ROCOF sensitive auxiliary signal model.

3.3 Frequency Responsive Modeling of BESS

EPRI CBEST model [57] is utilized in this thesis for BESS modeling. This model uses Voltage-Source Converter (VSC) for grid interfacing. In this topology, grid AC voltage V_{AC} is considered as battery terminal voltage. The amount of power going into and out of the battery is controlled by this voltage. Active power control strategy of BESS is demonstrated in Figure 3.4(a). Here P_{AUX} , P_{INIT} , I_{ACMAX} and P_{MAX} indicate the same quantities as of Figure 3.3(a).

Figure 3.4(b) illustrates the auxiliary power signal model of BESS, where various notations have same meaning as of Figure 3.3(b). The auxiliary power signal block of BESS is triggered by frequency deviation. The block generates an auxiliary power signal when frequency deviation exceeds a specified value. Eventually, the active power output of BESS is changed (increase/decrease) via this auxiliary power signal.

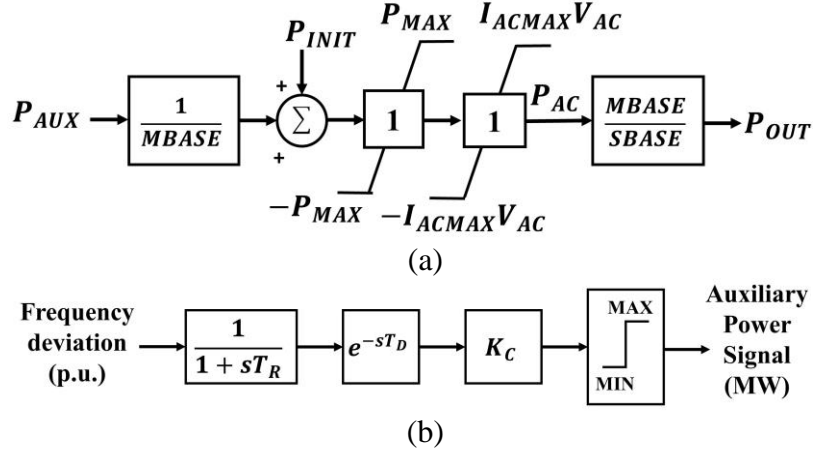


Figure 3.4: (a) Active power control block of BESS (b) Frequency deviation sensitive auxiliary signal model.

The amount of energy absorbed or supplied by the BESS E_{OUT} (in p.u.) depends on input and output efficiencies as shown in Fig. 5. The retrieval efficiency (OUT_{EFF}) is set to be 1.1 and storage efficiency (INP_{EFF}) is chosen to be 0.9 for achieving a turnaround efficiency of 80% [57].

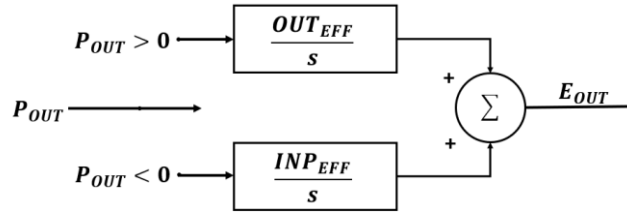


Figure 3.4: Energy control strategy of BESS.

3.4 Proposed Methodology

In this section, at first, analytical expressions are developed to find the sizes of SMES and BESS to ensure an adequate frequency response. Later on, a methodology is presented for coordinated action of these two ESS.

3.4.1 Sizing of SMES

Since SMES is utilized for short term storage support (i.e. inertial response only), the purpose of utilizing SMES is to restrict the value of ROCOF below the magnitude of maximum allowable limit R_{max} (in Hz/s) after a contingency. This condition can be expressed using (3).

$$ROCOF < R_{max} \quad (3)$$

Note that for a generation loss, ROCOF (df/dt) and maximum allowable ROCOF, both are negative since frequency declines with time. Thus, (3) can be rewritten considering signs of ROCOF and maximum allowable ROCOF.

$$-R_{max} < -ROCOF \quad (4)$$

According to the swing equation, following a contingency, ROCOF can be denoted using (5).

$$\frac{df}{dt} = \frac{f_o}{2IR} (\Delta P_g - \Delta P_L) \quad (5)$$

where f_o is the nominal system frequency (in Hz), IR denotes the system inertia (in MWs), ΔP_g means the change in generation (in MW) and ΔP_L refers to the change in system load (in MW). When n number of synchronous generators are committed, the total inertia IR can be quantified using (6) [58].

$$IR = \sum_{i=1}^n (S_i \times H_i) \quad (6)$$

where S_i specifies the rated MVA of i -th synchronous generator and H_i indicates the inertia constant of i -th synchronous generator (in s).

Further, following a loss of generation, ΔP_g can be expressed by (7), where $SMES_{size}$ is the required rated size of SMES (in MW) and g is the contingency size (in MW).

$$\Delta P_g = -g + SMES_{size} \quad (7)$$

Note that SMES is activated to provide inertial response only. Therefore, governor response (refer to Figure 3.1) is disregarded in this situation.

In addition, ΔP_L can be written using (8).

$$\Delta P_L = -k_p P_L \left(1 - \frac{f}{f_o} \right) \quad (8)$$

where P_L is the system load including loss (in MW) and k_p is load frequency relief. k_p provides the percentage of load change for every 1% change in system frequency [59]. Using (7) and (8) in (5), the swing equation becomes,

$$\frac{df}{dt} = \frac{f_o}{2IR} \left(k_p P_L \left(1 - \frac{f}{f_o} \right) - g + SMES_{size} \right) \quad (9)$$

Combining (4) and (9),

$$-R_{max} < \frac{f_o}{2IR} \left(k_p P_L \left(1 - \frac{f}{f_o} \right) - g + SMES_{size} \right) \quad (10)$$

By further simplifying, (10) can be rewritten as (11).

$$SMES_{size} > \left[g - \frac{2R_{max}IR}{f_o} - k_p P_L \left(1 - \frac{f}{f_o} \right) \right] \quad (11)$$

Therefore, (11) needs to be satisfied while determining the SMES size for rendering supplementary inertial response.

3.4.2 Sizing of BESS

As stated earlier, BESS can contribute to both IR and PFR following a power imbalance. However, in presence of a SMES, the BESS has relatively higher contribution in the primary frequency response segment compared to inertial response part (demonstrated later in results and analyses section). Accordingly, it is rational to consider frequency deviation thresholds for determining the optimal size of BESS. Thus, the objective of incorporating BESS according to this methodology is to keep the frequency above a predefined threshold f_{min} (in Hz). This condition can be expressed as (12).

$$f > f_{min} \quad (12)$$

where f is instantaneous system frequency (in Hz). When BESS is in action, it can provide primary frequency response along with inertial support. Thus, governor response functionality is also included in ΔP_g . Hence, ΔP_g is modified as shown in (13).

$$\Delta P_g = -g + \sum_{j=1}^{ng} \frac{f_o - f}{R} + BESS_{size} \quad (13)$$

where ng denotes the number of generators with active governors, which can provide primary frequency response according to droop R (in %). $BESS_{size}$ is the required rated size of BESS (in MW) to keep system frequency above a certain value. Using this modified expression of ΔP_g in (4), swing equation can be rewritten as (14).

$$\frac{df}{dt} = \frac{f_o}{2IR} \left[k_p P_L \left(1 - \frac{f}{f_o} \right) - g + BESS_{size} + f_o \sum_{j=1}^{ng} \frac{1}{R} \left(1 - \frac{f}{f_o} \right) \right] \quad (14)$$

For quantifying f , at first, expression of t is obtained by integrating both side of (14) with respect to dt .

$$t = - \frac{2IR}{k_p P_L + \left(f_o \sum_{j=1}^{ng} \frac{1}{R} \right)} \ln \left[1 - \left(1 - \frac{f}{f_o} \right) \frac{k_p P_L + \left(f_o \sum_{j=1}^{ng} \frac{1}{R} \right)}{g - BESS_{size}} \right] \quad (15)$$

Further, analytical expression of system frequency f can be obtained by solving (15). It is given by (16).

$$f = f_o \left[1 - \frac{g - BESS_{size}}{(k_p P_L + f_o \sum_{j=1}^{ng} \frac{1}{R})} \left(1 - e^{-\frac{t(k_p P_L + f_o \sum_{j=1}^{ng} \frac{1}{R})}}{2IR}} \right) \right] \quad (16)$$

In (16), system equivalent time constant T_s (in s) can be expressed by (17).

$$T_s = \frac{2IR}{\left(k_p P_L + f_o \sum_{j=1}^{ng} \frac{1}{R} \right)} \quad (17)$$

Using the expression of T_s in (16), system frequency can be further represented by (18).

$$f = f_o \left[1 - \frac{(g - BESS_{size})T_s}{2IR} \left(1 - e^{-\frac{t}{T_s}} \right) \right] \quad (18)$$

Let, frequency deviation following a contingency is ϕ (in p.u.), which can be expressed by (19).

$$\phi = \left(1 - \frac{f}{f_o} \right) \quad (19)$$

Combining (18) and (19), frequency deviation is provided by (20).

$$\phi = -\frac{(g - BESS_{size})T_s}{2IR} \left(e^{-\frac{t}{T_s}} - 1 \right) \quad (20)$$

In (20), the lowest value of $e^{-\frac{t}{T_s}}$ can be zero when t approaches infinite. When $e^{-\frac{t}{T_s}} = 0$, the highest value of frequency deviation after a contingency (ϕ_{max}) is found. Hence, ϕ_{max} is expressed via (21).

$$\phi_{max} = \frac{(g - BESS_{size})T_s}{2IR} \quad (21)$$

The minimum value of system frequency after a contingency i.e., frequency nadir (in Hz) is thus yielded by (22).

$$f_n = f_o - \phi_{max} f_o = f_o \left(1 - \frac{(g - BESS_{size})T_s}{2IR} \right) \quad (22)$$

Note that for keeping the system frequency above f_{min} , $f_n > f_{min}$ needs to be satisfied. Accordingly, highest allowable frequency deviation, denoted as ϕ_{max}' can be expressed using (23).

$$\phi_{max}' = \left(1 - \frac{f_{min}}{f_o} \right) \quad (23)$$

Thus, for satisfying (12), ϕ_{max}' must be greater than ϕ_{max} . It results in,

$$-\phi_{max}' < \frac{(-g + BESS_{size})T_s}{2IR} \quad (24)$$

Further modifying (24), expression of required BESS size can be found as follows.

$$BESS_{size} > \left(g - \frac{2IR\phi_{max}}{T_s} \right) \quad (25)$$

Using the expression of T_s in (25), analytical expression of required size of BESS can be derived. It is given by (26).

$$BESS_{size} > \left[g - \phi_{max}' \left(k_p P_L + f_o \sum_{j=1}^{ng} \frac{1}{R} \right) \right] \quad (26)$$

Therefore, (26) has to be satisfied while evaluating the BESS size for catering the desirable primary frequency response.

3.4.3 ESS Scheduling and Energy Rating

For scheduling the abovementioned ESS (i.e., SMES and BESS) in a power grid, certain constraints need to be satisfied. At first, State of Charge (SoC) values of these ESS are kept within a minimum and maximum range as shown in (27). This prevents the ESS to drain out completely. Violation of this safety limit can impact their lifetime and efficiency.

$$SoC_{min} \leq SoC_t \leq SoC_{max} \quad \forall t \quad (27)$$

where SoC_{min} and SoC_{max} are the minimum and maximum SoC limits respectively. Also, SoC_t is the SoC at any instant, which is defined by (28).

$$SoC_t = SoC_0 - \frac{1}{Q_c} \int I_{DC} dt \quad (28)$$

where SoC_0 refers to initial State of Charge, Q_c is amount charge (in C).

Next, ESS charging and discharging bounds need to be maintained. These conditions are given by (29)-(32) [60].

$$0 \leq P_{BESS,t}^{ch} \leq P_{BESS}^{chmax} \quad \forall t \quad (29)$$

$$0 \leq P_{SMES,t}^{ch} \leq P_{SMES}^{chmax} \quad \forall t \quad (30)$$

$$0 \leq P_{BESS,t}^{dch} \leq P_{BESS}^{dchmax} \quad \forall t \quad (31)$$

$$0 \leq P_{SMES,t}^{dch} \leq P_{SMES}^{dchmax} \quad \forall t \quad (32)$$

where $P_{BESS,t}^{ch}$ and $P_{BESS,t}^{dch}$ are the instantaneous amount of charge and discharge of BESS, $P_{SMES,t}^{ch}$ and $P_{SMES,t}^{dch}$ are the instantaneous amount of charge and discharge of SMES. Further, P_{BESS}^{chmax} and P_{SMES}^{chmax} denote the charging limits of BESS and SMES respectively. In addition, P_{BESS}^{dchmax} and P_{SMES}^{dchmax} refer to the discharging limits of BESS and SMES respectively.

By integrating the area under the power curve between ESS triggering instance and the first zero crossing, the amount of energy delivered by ESS can be obtained. Considering 10% tolerance margin and taking retrieval efficiency and storage efficiency into account, energy rating of an ESS can be expressed by (33).

$$E_{ESS} = \left[\int_{t_1}^{t_2} P_{out}(t) dt OUT_{EFF} + \int_{t_1}^{t_2} P_{out}(t) dt \frac{1}{INP_{EFF}} \right] 1.1 ESS_{size} \quad (33)$$

where t_1 is the triggering instance (in s), t_2 is the first zero crossing instance (in s), E_{ESS} is the energy rating of ESS (in J), P_{out} is the active power output of ESS (in p.u.) and ESS_{size} is the rated size of ESS (in MW). Note that both SMES and BESS are designed to provide 90% of the respective full capacities as the maximum output.

3.4.4 Proposed Strategy for Coordinated Action of ESS

In this subsection, a strategy is proposed for coordinated operation of SMES and BESS. In this strategy, SMES is activated by ROCOF and BESS is triggered by frequency deviation. A system operator can select the appropriate thresholds of ROCOF and frequency deviation based on system requirement.

The main objective of utilizing SMES is to preserve ROCOF within the maximum acceptable value R_{max} . Thus, SMES needs to be triggered before ROCOF reaches R_{max} . In addition, the target behind deploying BESS is to maintain system frequency above a certain threshold f_{min} . As such, the triggering frequency deviation of BESS, ϕ_t has to be less than the maximum allowable frequency deviation ϕ_{max}' .

The proposed algorithm for coordinated operation of SMES and BESS consists of multiple steps. For ease of understanding, the algorithm is depicted in Figure 3.5. The steps are described as follows.

Step-1: Model a low inertia power system having significant renewable penetration.

Step-2: Apply a considerably large contingency such as an interconnection trip or loss of a major generator.

Step-3: For a specific load scenario, via unit commitment scheduling, obtain the generation profile. Use this generation profile to calculate inertia using (6).

Step-4: Using this inertia value, calculate *ROCOF* via (5) for the applied contingency.

Step-5: Check if *ROCOF* exceeds the SMES triggering threshold R_t , where $R_t < R_{max}$. If yes, activate the SMES. If no, proceed to step 6. Note that *ROCOF*, R_t and R_{max} all denote magnitudes of corresponding rate of change of frequency.

Step-6: Calculate system frequency f using (18). Use $BESS_{size} = 0$ MW while calculating f . Note that this is the system frequency before including BESS.

Step-7: Calculate frequency deviation ϕ (in p.u.) using (19).

Step-8: Check if ϕ exceeds the BESS triggering frequency deviation ϕ_t (in p.u), where $\phi_t < \phi_{max}'$. If yes, activate BESS. Otherwise, conclude the process.

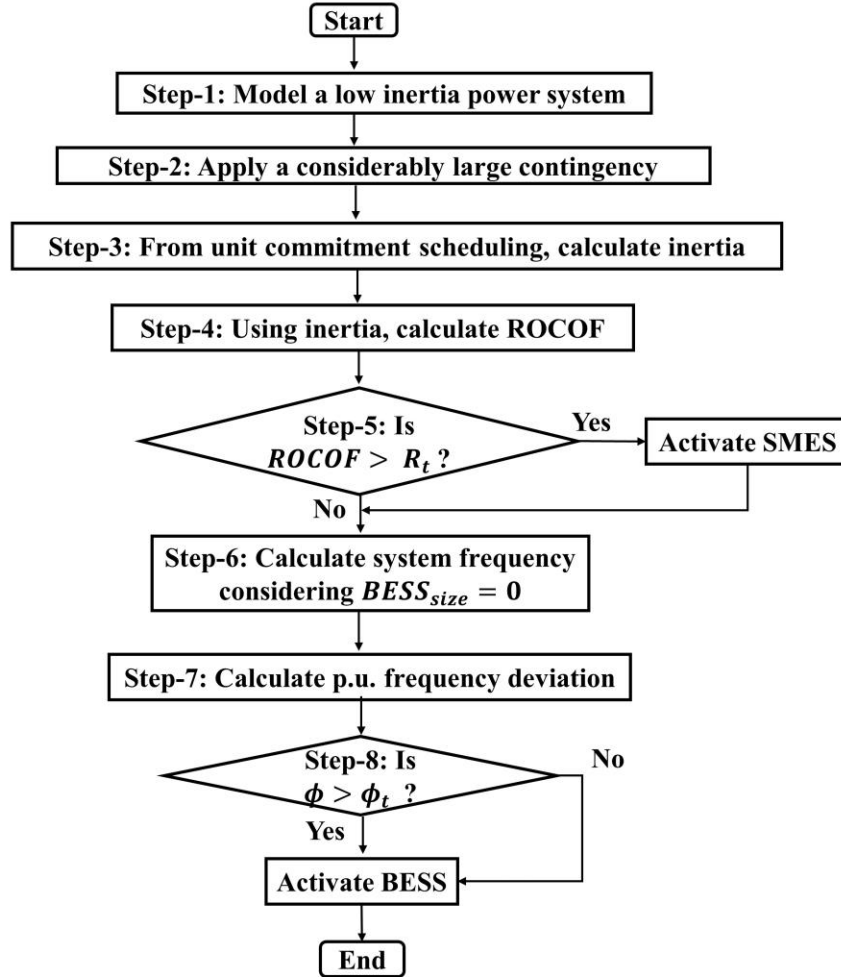


Figure 3.5: Proposed strategy for coordinated operation of SMES and BESS.

Note that this algorithm will be used by the transmission System Operator (TSO) to activate the ESS in case of a contingency. The values of frequency deviation and ROCOF thresholds are also under the jurisdiction of concerned TSO as these thresholds can vary depending on systems requirements, grid codes and energy policies of respective power systems.

To validate the competency of the proposed methodology, it entails to be verified through simulations. To this end, in the next section, the effectiveness of the proposed methodology is explored by applying it to the 59-bus South-East Australian power system.

3.5 Studied Power Grid and Simulation Scenarios

3.5.1 Studied Power System

The effectiveness of the proposed methodology is examined in a 50-Hz, 59 bus test network shown in Figure 3.6. This network is formed according to the South-East Australian 14-Generator Model [61]. Area-5 in Figure 3.6 depicts the low inertia grid, which virtually represents the equivalent high voltage transmission network of South Australia.

The number of conventional power plants has significantly reduced in South Australia due to substantial wind power penetration. Consequently, it can be treated as a classic case of a low inertia grid. A 275 kV HVAC interconnection links Area-5 with its adjacent network Area-3 (referred to Victoria).

Two conventional power plants are present in Area-5. These are called TPS_5 and PPS_5, which have multiple generating units. All the generating units have active governors. Table 3.1 outlines the necessary data of the conventional power plants.

Table 3.1: Conventional powerplant information

Power plant name	No. of units	Unit capacity (MW)	Unit MVA rating	Unit inertia constant (s)
TPS_5	4	250	333.0	4.0
PPS_5	6	125	166.6	7.5

The total installed wind generation capacity of Area-5 is assumed to be 1800 MW [62]. In the simulation network, wind power plants are placed at two locations – bus 508 and bus 509 to preserve similarity with the actual geographical positions of South Australian wind power plants. Wind power plants are modelled using Type 3 (DFIG) machines. In addition, SMES and BESS are connected to bus 501. All the dynamic simulations are performed using PSS[®]E software [63]. This software is extensively used all over the world to study the dynamic responses of power systems. The simulations are carried out using a computer with the following specifications: Intel[®] core[™] i5-8250 CPU@ 1.7-3.4 GHz.

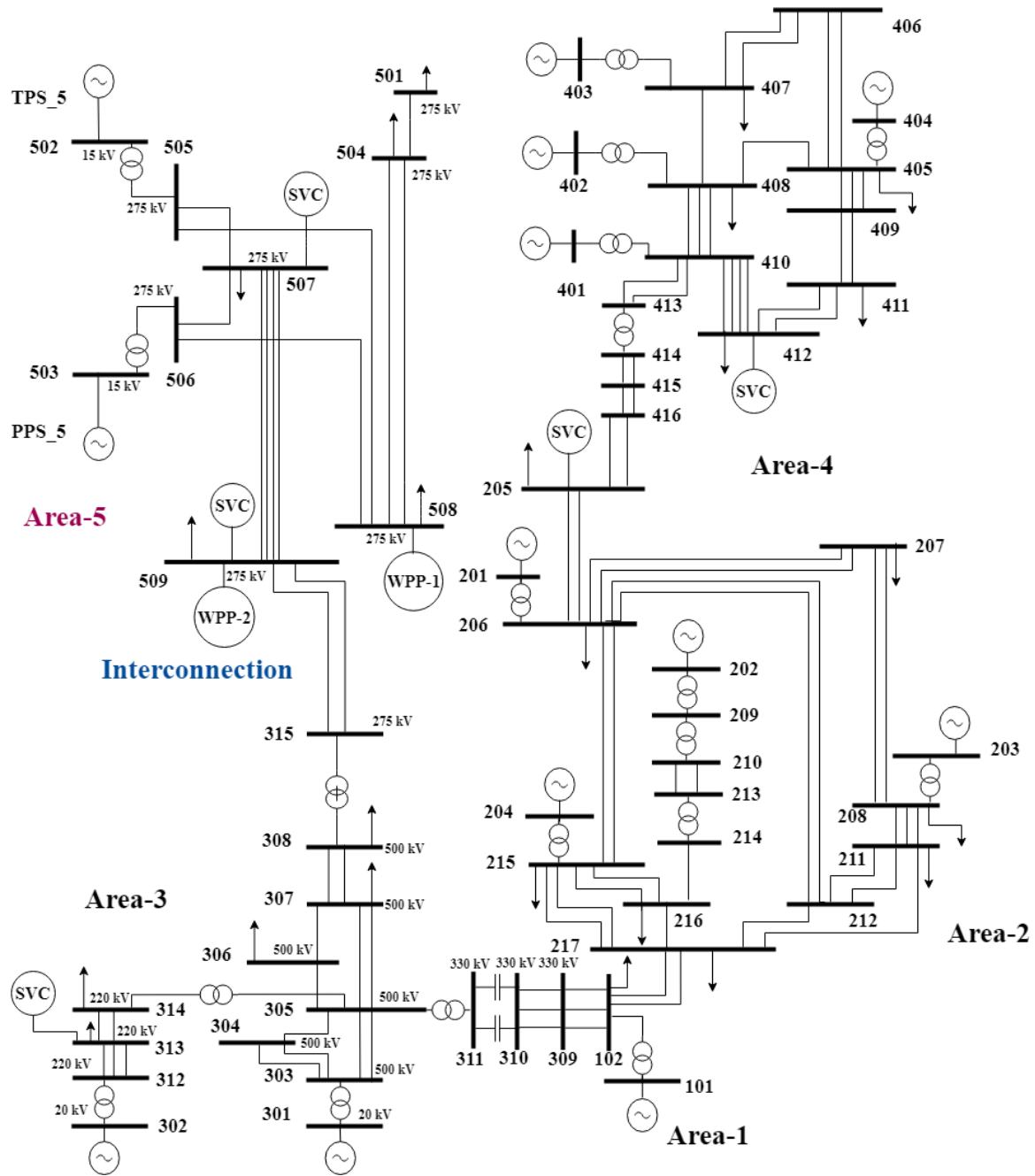


Figure 3.6: Single-line diagram of simulated power system.

3.5.2 Simulation Scenarios

To take into account various operating conditions, four different scenarios are investigated (denoted by Case study-I to Case study-IV). Note that during low load situation, a few synchronous generators are usually committed. Therefore, the frequency response deteriorates following a disturbance. As such, the total load in Area-5 is presumed to be 1450 MW in all simulation cases to represent a typical low load condition.

During simulation, it is assumed that Area-5 imports power from Area-3 via the interconnection. Frequency response of Area-5 is investigated following the interconnection trip. The number of committed synchronous generators in Area-5 is assumed to be 4 and 3 in various cases. In addition, power import through the interconnection is separately considered as 200 MW and 300 MW. Also, wind generation is varied to simulate different wind penetration levels. The simulation scenarios are outlined in Table 3.2.

Table 3.2: Simulation scenarios

Case study	No. of online synchronous generators	Synchronous generation (MW)	Wind generation (MW)	Inertia (MWs)	Interconnection import (MW)
I	4	679	625	5168	200
II	3	450	875	3834	200
III	4	679	525	5168	300
IV	3	450	775	3834	300

In addition, frequency response performances after adopting the proposed methodology are compared to that of two existing approach: Synchronous Condenser (SC) and “Only BESS”. For both of these systems, their rating is considered to be equal to the combined rating of SMES and BESS. Case studies I–IV are analyzed in three separate conditions, viz. without ESS, with ESS and with SC. For comparison purpose, it is assumed that the rating of SC is equal to the cumulative ratings of SMES and BESS. Simulation results and analyses are presented in the next section.

3.6 Results and Analyses

3.6.1 ESS Ratings

Using the proposed methodology, the ratings of SMES and BESS can be evaluated for any case studies. However, to keep the ratings reasonable yet worthwhile for low inertia situation, case study-II is considered as a baseline. Thus, the required SMES and BESS sizes are determined considering 3 online synchronous machines while the contingency size is 200 MW. Later on, the frequency response performances are analyzed after incorporating the estimated ESS.

3.6.1.1 SMES Size

The required SMES size can be determined from (11). The magnitude of maximum allowable ROCOF R_{max} is considered to be 1 Hz/s [64]. In case study-II, $IR= 3834$ MWs, $g= 200$ MW, $k_p = 1.5\%$ $P_L = 1450$ MW and $f_o = 50$ Hz. Hence, by using these values in (11), the minimum SMES rating is found to be around 47 MW.

3.6.1.2 BESS Size

The required BESS size can be determined from (26). The maximum allowable frequency deviation is assumed to be 1 Hz [65]. Subsequently, ϕ_{max}' is 0.02 p.u. using the base frequency of 50 Hz. The BESS size is also determined for case study-II. Thus, by using $g= 200$ MW, $f_o = 50$ Hz, $R=5\%$, $k_p= 1.5\%$ and $P_L= 1450$ in (26), the minimum BESS rating is around 97 MW.

Based on the above ratings of SMES and BESS, the SC rating is found to be 144 MVA. Thus, a 144 MVA SC is assumed to be connected to the grid for frequency response comparison. Similarly, for “Only BESS” system, the rating of the BESS is considered to be 144 MW.

3.6.2 Improvement of Frequency Response

Following the contingency, frequencies of online generators are noted. Then, center of frequency (f) is determined using (34) to eliminate small variation in frequencies of different generators.

$$f = \frac{\sum_{i=1}^{i=n}(f_i \times S_i \times H_i)}{\sum_{i=1}^{i=n}(S_i \times H_i)} \quad (34)$$

where f_i is the frequency of $i - th$ synchronous generator (in Hz).

For all case studies, it is assumed that SMES (rated capacity: 47 MW) is activated when ROCOF after the contingency exceeds 0.5 Hz/s. Further, BESS (rated capacity: 97 MW) is activated when the frequency goes below 49.9 Hz, i.e., frequency deviation exceeds 0.1 Hz (i.e., 0.002 p.u.).

When frequency falls below a certain threshold, the UFLS mechanism is triggered. In this work, it is assumed that the UFLS scheme consists of three stages. The corresponding activation frequencies of these stages are 49 Hz, 48.75 Hz and 48.5 Hz. Also, the UFLS scheme is set to shed 5%, 10% and 15% of the total load at the 1st, 2nd and 3rd stages respectively. Frequency response performances in various case studies are presented as follows.

3.6.2.1 Case Study-I

In this case study, 4 synchronous machines are online and the interconnection is tripped while importing 200 MW power from Area-3. The frequency response curve is shown in Figure 3.7(a). Following this contingency, ROCOF is quantified to be 0.96 Hz/s. Hence, ROCOF crosses the 0.5 Hz/s threshold and SMES with a rated capacity of 47 MW is activated. SMES output power is depicted in Figure 3.7(b), which necessarily represents an emulated inertial response.

Frequency nadir is 48.98 Hz (without ESS) as depicted by the red trace in Figure 3.7(a). Thus, the frequency deviation is 0.0204 p.u., which surpasses the activation threshold of BESS. Consequently, BESS with a rated capacity of 97 MW is activated as shown in Figure 3.7(c). It is seen that the BESS output power increases at first when frequency declines. Afterwards, BESS output decreases slowly due to increase in frequency after the nadir point. When the frequency stabilizes completely (not shown in Figure 3.7(c)), then the BESS output also becomes constant. After around 15-30 minutes, Tertiary Frequency Response (TFR) re-dispatches the generator outputs and brings the system frequency to its nominal value. At that instance, BESS output becomes zero. Figure 3.7(c) also justifies the sizing of BESS by considering its PFR contribution. It can be seen that BESS provides around 63 MW active power during IR and 91 MW during PFR when a SMES is also online. Note that a BESS of 97 MW capacity can certainly deliver 63 MW power but not vice-versa.

As UFLS initiates at 49 Hz, system encounters load shedding before utilizing SMES and BESS. The amount of load shedding is 73 MW without ESS. After incorporating both ESS, ROCOF becomes 0.50 Hz/s and frequency nadir becomes 49.61 Hz. Thus, the ROCOF stays below the allowable limit of 1 Hz/s. Furthermore, the frequency excursion stops well above 49 Hz. Consequently, load shedding can be fully avoided after deploying the ESS.

Note that according to (20), the lowest point in the frequency response curve should occur when t is too larger than T_s . However, in Figure 3.7(a), the frequency starts to increase after around 4.6s. The reason behind this is after reaching the frequency nadir point, due to additional active power support from SMES and BESS, the total generation surpasses the system load. As a result, the frequency starts to rise before load-generation balance is achieved.

If a synchronous condenser is incorporated instead of ESS, the ROCOF becomes 0.87 Hz/s due to inertial support from SC. However, frequency nadir still stays below 49 Hz (depicted by the blue trace) and system encounters 73 MW load cut. Thus, frequency response significantly improves when the proposed strategy is implemented.

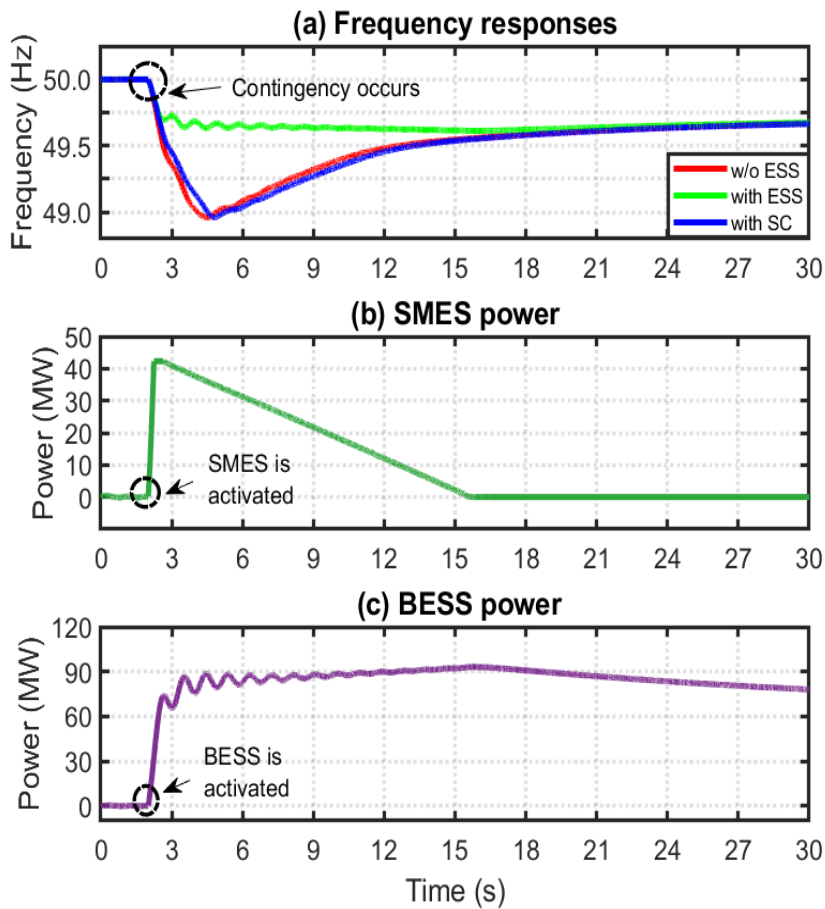


Figure 3.7: (a) Frequency response in case study - I (b) SMES output in case study - I (c) BESS output in case study – I.

3.6.2.2 Case Study-II

In this case, 200 MW interconnection trip is applied as a contingency while 3 machines are online. For this contingency, ROCOF becomes 1.29 Hz/s. Thereby, ROCOF exceeds the SMES triggering threshold of 0.5 Hz/s. Accordingly, SMES gets activated.

In addition, the frequency nadir without ESS is 48.82 Hz as shown by the red line in Figure 3.8(a). Hence, frequency deviation is 0.0236 p.u., which is more than the BESS activation threshold. As a result, BESS is enabled. Consequently, frequency response improves as depicted by the green trace in Figure 3.8(a), and frequency nadir becomes 49.50 Hz. Also, ROCOF is found to be 0.57 Hz/s, which stays below the safety limit. The SMES output power is shown in Figure 3.8(b) and BESS output power is illustrated in Figure 3.8(c).

Note that before activating ESS, frequency falls below 49 Hz. As a result, system incurs 73 MW load shedding. However, frequency excursion stops above 49 Hz after including ESS. Consequently, load shedding is completely averted. When SC is connected instead of ESS,

ROCOF is found to be 1.13 Hz/s and frequency nadir is found to be 48.85 as depicted by the blue trace in Figure 3.8(a). Hence, neither the ROCOF stays above the 1 Hz/s safety limit, nor the UFLS is averted. Therefore, unlike proposed ESS, inclusion of SC does not provide satisfactory frequency response performance. In other words, the proposed method outperforms the existing approach.

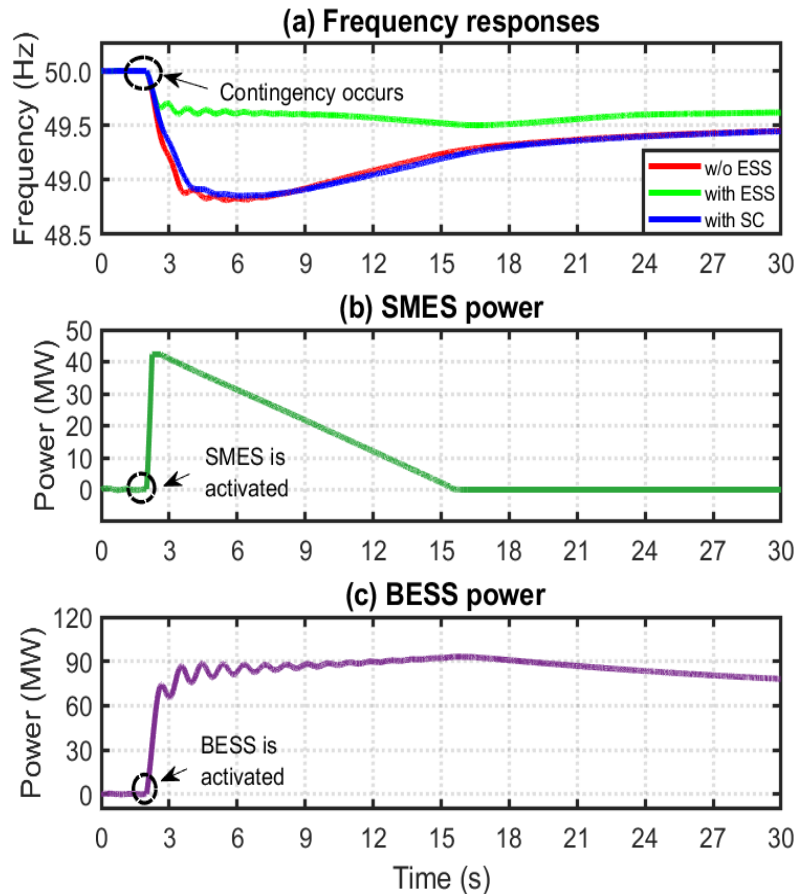


Figure 3.8: (a) Frequency response in case study- II (b) SMES output in case study- II (c) BESS output in case study –II.

3.6.2.3 Case Study-III

In this case, the number of committed synchronous machines is 4 and 300 MW interconnection trip is applied as a contingency. After the loss of interconnection, ROCOF becomes 1.44 Hz/s. In addition, frequency nadir is 48.68 Hz (red line in Figure 3.9) when no ESS is incorporated. Thus, the frequency deviation is 1.32 Hz (0.0264 p.u.). As both ROCOF and frequency deviation exceed the respective triggering thresholds, SMES and BESS are activated. After enabling both ESS, ROCOF is quantified to be 0.81 Hz/s. Thus, ROCOF is confined to the maximum limit. In addition, the frequency nadir becomes 48.98 Hz as illustrated

by the green trace in Figure 3.9. SMES and BESS outputs have the same shapes as of Figures 3.8(b) and 3.8(c).

Before activating ESS, the network experiences 217 MW load shedding. However, it becomes 73 MW when both ESS are enabled. Note that load shedding is not fully stopped because ESS ratings are determined considering 200 MW contingency. Nevertheless, significant reduction in load shedding (144 MW) is achieved when SMES and BESS are instigated. It is to be pointed out that to completely avoid UFLS, ESS sizes needs to be re-estimated for 300 MW contingency. However, ratings would increase in this case, which may cause financial concern for system operators.

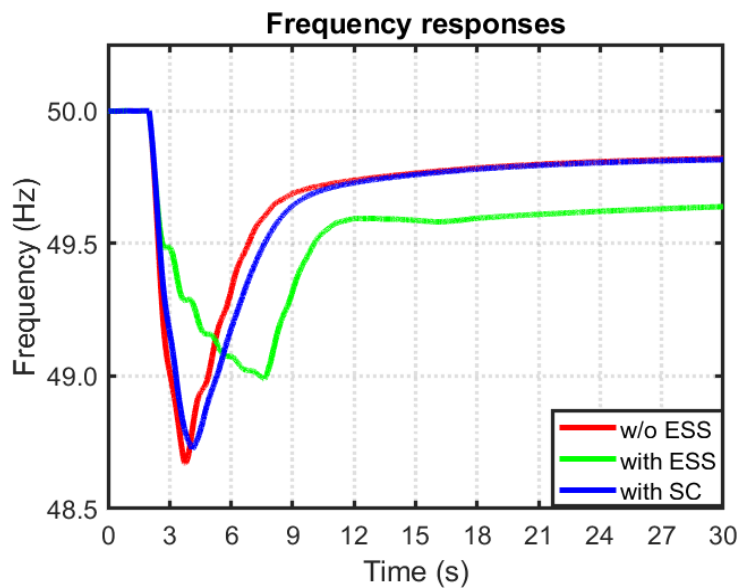


Figure 3.9: Frequency response in case study- III.

Further, when SC is deployed instead of ESS, ROCOF becomes 1.30 Hz/s and frequency nadir becomes 48.73 Hz. Hence, ROCOF exceeds the safety limit and system incurs 217 MW UFLS. Thus, incorporation of SC provides unsatisfactory frequency response.

3.6.2.4 Case Study-IV

In this case, 3 synchronous machines are committed and the contingency size is 300 MW. Following the interconnection trip, when no ESS is present, ROCOF is found to be 1.94 Hz/s. Also, frequency nadir is 48.63 Hz (which corresponds to 0.0274 p.u. frequency deviation) as depicted by the red line in Figure 3.10. Since both ROCOF and frequency deviation surpass respective activation thresholds, both ESS are triggered. Due to supplementary inertia and primary frequency response, frequency excursion improves as shown by the green trace in Figure 3.10. It is found that ROCOF reduces to 0.98 Hz/s and the frequency nadir improves to 48.94 Hz after including ESS. Furthermore, load shedding amounts are 217 MW and 73 MW

without and with ESS respectively. Therefore, load shedding reduces by 144 MW when SMES and BESS are simultaneously deployed.

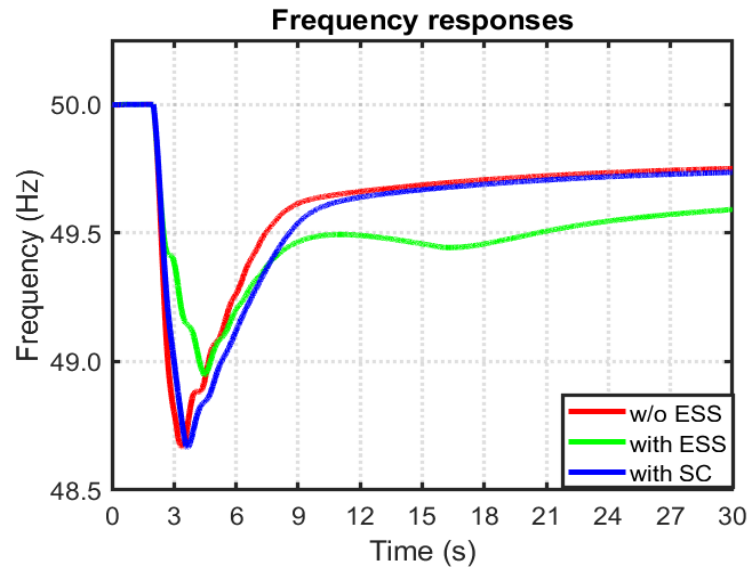


Figure 3.10: Frequency response in case study- IV.

In addition, inclusion of SC as an alternative to ESS yields a ROCOF of 1.70 Hz/s and frequency nadir of 48.64 Hz. As a result, system incurs 217 MW load shedding. Thus, neither ROCOF stays below the safety limit nor UFLS is mitigated by SC incorporation.

3.6.3 Comparison With “Only BESS”

In this subsection, the performance of the proposed strategy is compared with “Only BESS” where a BESS of 144 MW capacity is installed instead of the proposed ESS. For the four cases illustrated in Table 3.2, system frequency response is studied for proposed ESS and “Only BESS”.

3.6.3.1 Case Study-I

As stated earlier, in this case study, 4 synchronous machines are online and the interconnection is tripped while importing 200 MW power from Area-3. The frequency response curves for this case are shown in Figure 3.11. The frequency response curves illustrate that following the contingency, with proposed ESS, ROCOF is 0.50 Hz/s and frequency nadir is 49.61 Hz (Red trace). Whereas with an “Only BESS”, the ROCOF is found to be 0.52 Hz/s and frequency nadir is found to be 49.51 Hz (Black trace). Thus, the proposed strategy yields slightly better performance than that of “Only BESS”.

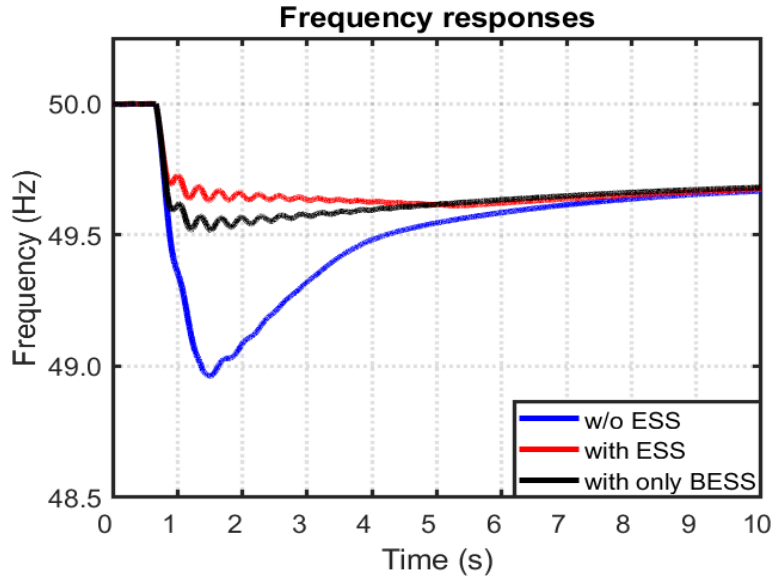


Figure 3.11: Frequency response in case study- I.

3.6.3.2 Case Study-II

The frequency response curves for case study-II are portrayed in Figure 3.12. The frequency response curves show that following the trip of the 200 MW interconnection, with proposed ESS, ROCOF is 0.57 Hz/s and frequency nadir is 49.50 Hz (Red trace). Nevertheless, with “Only BESS”, the ROCOF is found to be 0.58 Hz/s and frequency nadir is found to be 49.48 Hz (Black trace). Thus, the proposed strategy yields almost similar performance compared to that of “Only BESS”.

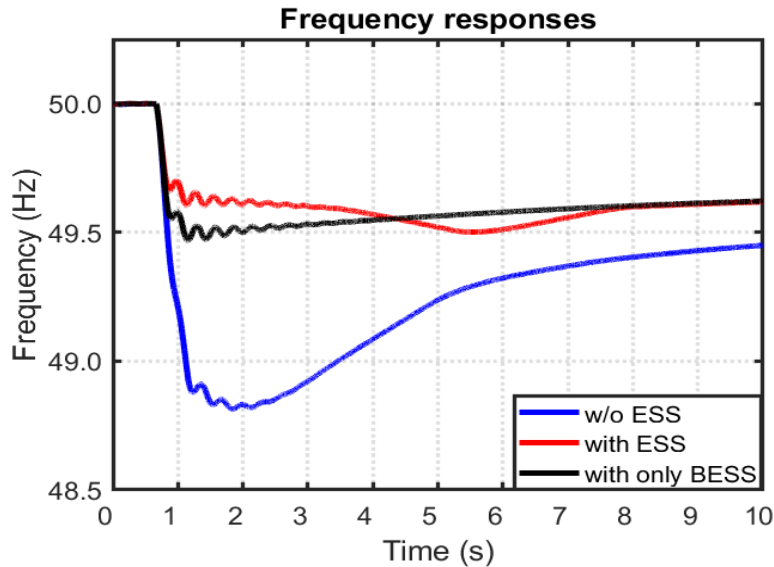


Figure 3.12: Frequency response in case study- II.

3.6.3.3 Case Study-III

As articulated in the previous subsection, in this case study, 4 synchronous machines are online and the interconnection is tripped while importing 300 MW power from Area-3. The frequency response curves for this case are shown in Figure 3.13.

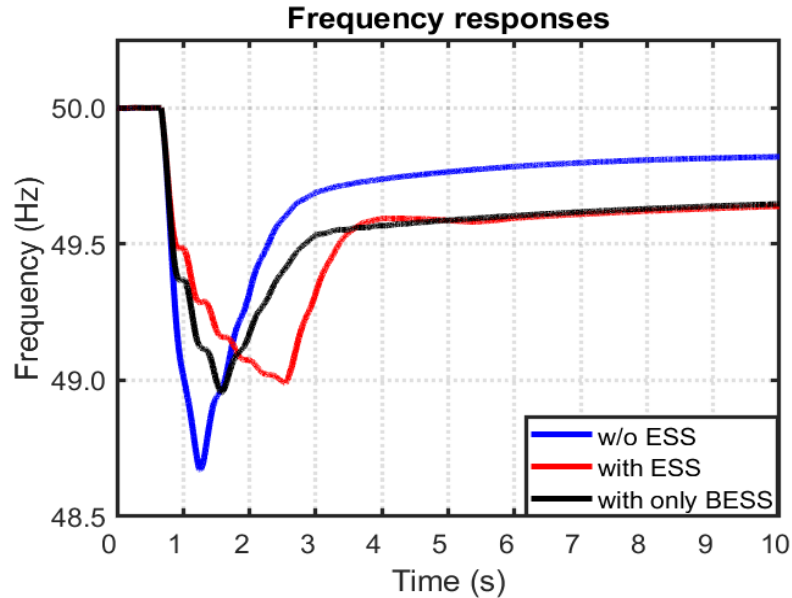


Figure 3.13: Frequency response in case study- III.

The frequency response curves illustrate that following the contingency, with proposed ESS, ROCOF is 0.81 Hz/s and frequency nadir is 48.98 Hz (Red trace). When “Only BESS” is considered instead of the proposed strategy, the ROCOF is found to be 0.87 Hz/s and frequency nadir is found to be 48.94 Hz (Black trace). In case of both strategies, 73 MW of load is shed. Thus, again the proposed strategy yields a slightly better system response than that of “Only BESS”.

3.6.3.4 Case Study-IV

In this case study, 3 synchronous machines are online and the interconnection is tripped while importing 300 MW power from Area-3 as stated in the earlier subsection. According to the frequency response curves shown in Figure 3.14, following the loss of 300 MW power import, with proposed ESS, ROCOF is 0.98 Hz/s and frequency nadir is 48.94 Hz (Red trace). However, if “Only BESS” is incorporated, the ROCOF is found to be 1.02 Hz/s and frequency nadir is found to be 48.92 Hz (Black trace). Note that for “Only BESS”, the system ROCOF goes beyond the 1 Hz/s safety limit. Nevertheless, for both strategies, again 73 MW of UFLS is occurred. Therefore, the case studies illustrates that the proposed methodology renders slightly superior system response compared to that of “Only BESS”.

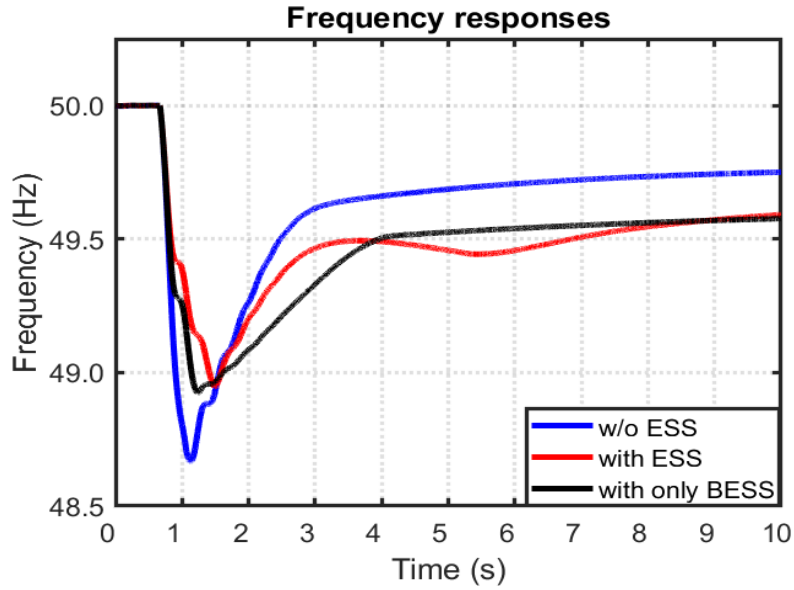


Figure 3.14: Frequency response in case study- IV.

For ease of comparison, simulation results and quantities of load shedding are summarized in Table 3.3 and Table 3.4 respectively.

It is evident from the above analyses that the proposed strategy significantly improves the frequency response of the low inertia grid. As such, ROCOF is restricted below the maximum allowable limit and the amount of load shedding considerably reduces when SMES and BESS are activated in a coordinated manner. In addition, the proposed methodology outperforms both SC and “Only BESS” strategy in terms of frequency response adequacy.

Table 3.3: Summary of the simulation results

Case study	No. of online synchronous generators	Contingency size (MW)	ROCOF magnitude (Hz/s)				Frequency nadir (Hz)			
			Without ESS	With SC	With only BESS	With ESS	Without ESS	With SC	With only BESS	With ESS
I	4	200	0.96	0.87	0.52	0.50	48.98	48.99	49.51	49.61
II	3	200	1.29	1.13	0.58	0.57	48.82	48.85	49.48	49.50
III	4	300	1.44	1.30	0.87	0.81	48.68	48.73	48.94	48.98
IV	3	300	1.94	1.70	1.02	0.98	48.63	48.64	48.92	48.94

Table 3.4: Summary of the load shedding amounts

Case study		I	II	III	IV
Load shedding (MW)	Without ESS	73	73	217	217
	With SC	73	73	217	217
	With only BESS	0	0	73	73
	With ESS	0	0	73	73

3.7 Further Discussions

3.7.1 Benefits of The Analytical Approach

The benefits of the proposed analytical derivations to find the minimum ratings of BESS and SMES are as follows.

- The developed analytical expressions take into account the crucial system parameters such as system frequency deviation, system ROCOF, inertial response and governor response of online synchronous generators for determining minimum ratings of ESS.
- It reduces the dependency on time consuming time-domain simulations and complex optimization algorithms. These algorithms mainly focus on profit maximization instead of power system dynamics while evaluating the ratings of ESS.
- Unlike existing approaches, no linearization of swing equation is done to determine the system frequency. As such, the dynamic attributes of frequency excursion is captured in the proposed analytical derivations.

3.7.2 Applicability of The Proposed Method

It is to be noted that SMES and BESS both have the capacity to charge and discharge at a very rapid rate. In this thesis, the ESS is utilized for under frequency situation where additional active power support is provided by the ESS by discharging rapidly. However, situations can arise where a system is exporting a significant amount of power to its adjacent area and suddenly the interconnection among these two areas trips. As a result, frequency of the power-exporting area can increase and even cross the safety limits [65]. In that case, ESS will be charged to absorb the surplus active power [66]. Thus, the proposed methodology can resolve over frequency issue in renewable dominated grids.

It is to be noted that the proposed methodology will be applied by the TSO during the planning stage to determine the ratings of ESS. According to the grid code, the TSO will choose

the threshold values of ROCOF and frequency nadir, which are required for calculating the minimum ratings of the ESS. Afterwards, the ESS can be installed and dispatched accordingly. However, the strategy illustrated in Figure 3.6 will be applied by the TSO during operational stage of a power grid. As stated previously, the threshold values for activating SMES and BESS are under the jurisdiction of the concerned TSO. These threshold values can be altered according to the grid requirements. In addition, the thresholds may need to be modified for conforming to the constraints imposed by regulatory bodies.

In this thesis, variable speed wind turbine generators are considered, which are decoupled from the grid via converters. Therefore, these wind generators usually offer insignificant inertia and governor response when no additional control algorithm is adopted. Likewise, solar photovoltaic (PV) generators are isolated from the network via power electronics interfaces. Hence, a power system under high PV penetration faces similar frequency response challenges as of a wind dominated grid. Therefore, the methodology demonstrated in this paper can also be applied to PV-rich power systems.

3.7.3 Factors Influencing ESS Response

It is necessary to ensure that the installed ESS will work properly maintaining its expected response speed. However, few factors can influence the ESS performance and can lead to undesirable response. The following requirements need to be fulfilled for ensuring safe and effective performance of the ESS [67].

- The ESS should be able to fulfill the requirements of enhanced frequency response and PFR, which can vary according to the regulation imposed by concerning TSO [68]. By maintaining the SOC management among service windows, according to the National Grid, the ESS should be able to respond within 1 s of the disturbance to provide frequency response [69]. In addition, dedicated ESS for PFR should be able to respond within 10 s of an under-frequency event [69].
- The ESS must be able to deliver or absorb active power thus ensuring delivery in either direction (import to/ export from the host grid).
- The service provider should be able to deliver 100% capacity of the ESS for a minimum of 15 minutes (Supplementary frequency support duration).
- Material quality and cost, energy contents and condition of cell degradation of concerning storages must be analyzed properly.
- The ESS must be able to fulfill its service capability by effectively managing its SoC.

3.8 Summary

In this chapter, extensive investigations are carried out to explore the roles of SMES and BESS for improving the frequency response of a low inertia grid. To this end, analytical expressions are developed for evaluating the minimum ratings of SMES and BESS. Notably, the proposed sizing scheme for ESS has some advantages over its recent counterparts such as reduced dependency on time-domain simulations and time consuming heuristic optimization algorithms and consideration of crucial system operating parameters. Also, a methodology is proposed for coordinated operation of these two ESS. The ratings of SMES and BESS are assessed considering 3 online synchronous machines while the interconnection tripping size is 200 MW. For this contingency, the minimum SMES and BESS ratings are found to be approximately 47 MW and 97 MW respectively to keep ROCOF and frequency deviation within the given acceptable limits.

Frequency response performances are analyzed in four different case studies following the loss of interconnection. Without incorporating ESS (i.e., SMES and BESS), ROCOF is close to or more than 1 Hz/s. Also, the frequency nadirs are less than 49 Hz. Consequently, system encounters significant under frequency load shedding. In contrast, when ESS are activated, ROCOF is confined to the maximum allowable limit of 1 Hz/s. Furthermore, the frequency nadirs are above 49 Hz (in 200 MW contingency) or very close to 49 Hz (in 300 MW contingency). As a result, load shedding is either fully averted or significantly minimized.

When synchronous condenser (SC) is placed instead of ESS, the ROCOF shows an improving trend due to additional inertial support. However, in three case studies, SC fails to keep ROCOF below the safety threshold. In addition, inclusion of SC does not reduce the amount of load shedding in any case study. When only BESS is incorporated, it yields slightly inferior system performance than that of the proposed methodology. Therefore, it can be revealed that the proposed methodology yields adequate frequency response to make a low inertia grid more secure and resilient. Finally, it is worth stating that the developed technique can be applied to any power system to enhance renewable power penetration by retaining satisfactory frequency response.

Chapter 4

Modeling and Utilization of TCSC for Enhancing Frequency Response

In this chapter, firstly, a brief insight into the frequency responsive modeling of TCSC is outlined. Later on, the proposed methodology to determine the optimal TCSC parameters to avert the risk of cascading contingency as well as subsequent blackout is discussed. Furthermore, an analytical methodology to determine maximum wind penetration level is discussed. Afterwards, simulation scenarios are formed and investigated accordingly. Performance comparison with an existing technology is also provided afterwards.

4.1 Frequency Responsive Modeling of TCSC

TCSC is typically placed in series with a transmission line to reduce the reactance of the line [40]. A TCSC essentially consists of a series compensator, which includes a fixed capacitor in parallel with a thyristor and a controllable reactor [42, 45]. Basic configuration of this device is illustrated in Figure 4.1. The reactance can be decreased by altering the thyristor firing angles. As such, the real power carrying capacity of the transmission line improves.

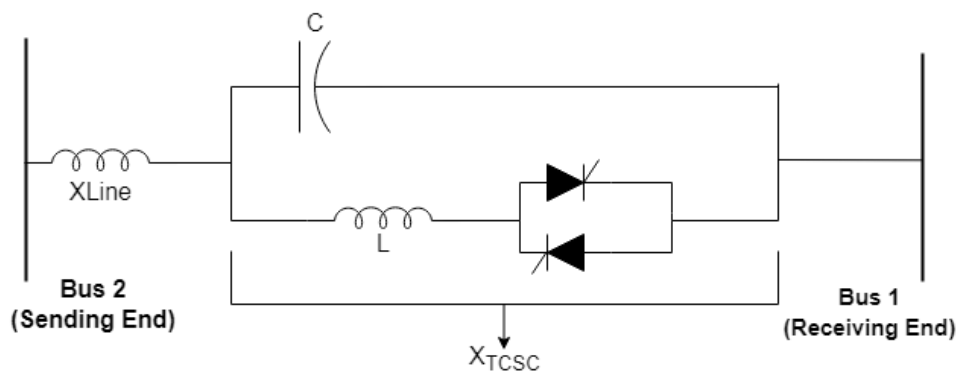


Figure 4.1: Basic configuration of TCSC

In general, TCSC is placed in series with the interconnection (i.e., tie-line) between two adjacent areas. Let us assume that the associated buses are – bus 2 (sending end) and bus 1 (receiving end). Suppose V_2 is the sending end voltage magnitude (in p.u), V_1 is the receiving end voltage magnitude (in p.u), δ_2 is the sending end voltage angle (in degree), δ_1 is the receiving end voltage angle (in degree), δ is angle difference between sending and receiving end voltages (in degree), X_L is the inductive reactance (in Ω) and X_C is the capacitive reactance

of TCSC (in Ω), X_{Line} is the total reactance of the tie-line without TCSC (in Ω), X_{TCSC} is the total reactance of TCSC (in Ω). Thus, tie-line power flow in presence of TCSC can be expressed by (35) and (36) [45].

$$P_{tie} - jQ_{tie} = V_2^* i_{Line} \quad (35)$$

$$P_{tie} - jQ_{tie} = [|V_2| \angle -\delta_2] \left[\frac{|V_2| \angle \delta_2 - |V_1| \angle \delta_1}{|X_{Line} - X_{TCSC}| \angle 90^\circ} \right] \quad (36)$$

From (37), the real power flow through the tie-line can be obtained as follows.

$$P_{tie} = \frac{|V_2||V_1|}{(X_{Line} - X_{TCSC})} \sin(\delta_2 - \delta_1) \quad (37)$$

Let, $k_c = \frac{X_{TCSC}}{X_{Line}}$ be the compensation factor of the TCSC. Using the value of k_c and applying partial decomposition method, (37) can be rewritten as (38).

$$P_{tie} = \frac{|V_2||V_1|}{(X_{Line})} \sin(\delta_2 - \delta_1) + \left(\frac{k_c}{1 - k_c} \right) \frac{|V_2||V_1|}{(X_{Line})} \sin(\delta_2 - \delta_1) \quad (38)$$

Note that changes in δ_2, δ_1 and k_c are small from their initial values – δ_2^0, δ_1^0 and k_c^0 respectively. Here, ‘initial’ implies the operating condition before TCSC is activated. Therefore, (38) can be rearranged as (39).

$$\Delta P_{tie} = \left[\frac{|V_2||V_1|}{(X_{Line})} \cos(\delta_2^0 - \delta_1^0) (\Delta\delta_2 - \Delta\delta_1) \right] + \left(\frac{\Delta k_c}{1 - \Delta k_c} \right) \frac{|V_2||V_1|}{(X_{Line})} \sin(\delta_2^0 - \delta_1^0) \quad (39)$$

Assuming, $T_{Line}^0 = \frac{|V_2||V_1|}{(X_{Line})} \cos(\delta_2^0 - \delta_1^0)$ and $A = \frac{|V_2||V_1|}{(X_{Line})} \sin(\delta_2^0 - \delta_1^0)$, Eq. (7) can be rewritten as (40).

$$\Delta P_{tie} = T_{Line}^0 (\Delta\delta_2 - \Delta\delta_1) + \frac{\Delta k_c A}{1 - \Delta k_c} \quad (40)$$

By definition, $\Delta\delta_2 = 2\pi \int (f_2 dt)$ and $\Delta\delta_1 = 2\pi \int (f_1 dt)$. Thus, after Laplace transform, (40) can be expressed by (41).

$$\Delta P_{tie}(s) = 2\pi T_{Line}^0 \frac{(\Delta f_2(s) - \Delta f_1(s))}{s} + \frac{\Delta k_c A}{1 - \Delta k_c} \quad (41)$$

Applying Taylor series expansion and modifying,

$$\Delta P_{tie}(s) = \Delta P_{tie}^0(s) + \Delta P_{TCSC}(s)A \quad (42)$$

Thus, total change in tie-line flow can be expressed as a summation of change in initial tie-line flow and change in tie-line flow due to TCSC installation. The real power flow through the tie-line (i.e., interconnection) can be controlled based on (42). For this purpose, a frequency-responsive TCSC model can be utilized. To this end, the transfer function representation of TCSC as shown in Figure 4.2 is taken into consideration.

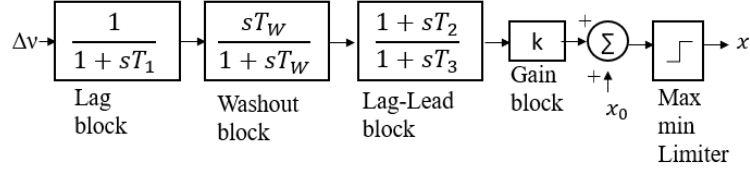


Figure 4.2: Block diagram of a frequency responsive TCSC

The input Δv is the normalized speed deviation (i.e., frequency deviation) of a synchronous machine, which is connected to a nearby bus where TCSC is placed. The output signal x is the final reactance of the tie-line. The tunable parameters of TCSC are T_2 , T_3 and k . The max-min limiter is used for confining the reactance value within a specific range selected by a system operator.

The TCSC model can be expressed by the following set of state equations. when washout stage is neglected [70].

$$\Delta \dot{\alpha} = -\frac{\Delta \alpha}{T_3} - \frac{k}{\omega_s} \frac{1}{T_3} (\Delta \omega) - \frac{k T_2}{\omega_s T_3} (\Delta \dot{\omega}) \quad (43)$$

$$\dot{x} = -\frac{\Delta \alpha}{T_1} - \frac{1}{T_1} x \quad (44)$$

where $\Delta \alpha$ is the change in firing angle (in degree), T_1 , T_2 , and T_3 are time constants (in s), ω_s is the rated speed of the machine (in rad/s) and $\Delta \omega$ is the speed deviation following a contingency (in rad/s).

The firing angle can alter the equivalent reactance of the TCSC according to (45) [71].

$$\begin{aligned} X_{tcsc} = & -X_c + C_1(2(\pi - \alpha) + \sin(2(\pi - \alpha))) \\ & - C_2 \cos^2(\pi - \alpha) \times (\bar{\omega} \tan(\bar{\omega}(\pi - \alpha)) \\ & - \tan(\pi - \alpha)) \end{aligned} \quad (45)$$

where $X_{LC} = \frac{X_C X_L}{X_C - X_L}$, $C_1 = \frac{X_C + X_{LC}}{\pi}$, $C_2 = \frac{4X_{LC}^2}{\pi X_L}$ and $\bar{\omega} = \sqrt{X_C/X_L}$. From (45), the linearized TCSC equivalent reactance can be expressed by (46) [51].

$$\begin{aligned} \Delta X_{tcsc} = & -2C_1(1 + \cos(2\alpha)) \\ & + C_2 \sin(2\alpha) (\bar{\omega} \tan(\bar{\omega}(\pi - \alpha)) - \tan \alpha) \\ & + C_2 \left(\frac{\bar{\omega}^2 (\cos^2(\pi - \alpha))}{\cos^2(\bar{\omega}(\pi - \alpha))} - 1 \right) \Delta \alpha \end{aligned} \quad (46)$$

Depending on frequency deviation, firing angle changes as suggested by (46). Change in firing angle ultimately controls the TCSC equivalent reactance, which is evident from (46). Eventually, the frequency responsive design of TCSC is achieved which can be utilized to avert the risk of network separation.

In the subsequent section, the procedure for optimally selecting the TCSC parameter is discussed. In addition, an analytical expression is developed to determine the enhancement of maximum wind penetration level after incorporating TCSC.

4.2 Proposed Methodology

In this section, at first, a strategy is established to find the optimal parameters of the TCSC. Afterwards, an analytical expression is derived to evaluate the increase in maximum wind power penetration level when TCSC is incorporated.

4.2.1 Finding Optimal Parameters of TCSC

For determining the most appropriate parameters of the TCSC, Particle Swarm Optimization (PSO) algorithm [72] is utilized in this study. In the beginning of this algorithm, it initializes M number of random swarm particles, having R number of unknown parameters to be optimized. Here, each particle refers to a potential solution. After every iteration, according to the given fitness equation, fitness of every particle is evaluated. Every particle is given a definite velocity and the particles flow through the problem space. While travelling through the problem space, the particles keep the memory of its previous best position (denoted by P_{best}) and fitness. The particle, for which the maximum fitness value is obtained, is called global best (G_{best}) of the swarm. The target is to accelerate the particles towards P_{best} and G_{best} locations. The velocity and position of each particle is governed by (47) and (48) respectively.

$$v_{id}(m) = wv_{id}(m-1) + acc_1rand_1(G_{best} - P_{id}(m-1)) + acc_2rand_2(P_{best_i} - P_{id}(m-1)) \quad (47)$$

$$P_{id}(m) = P_{id}(m-1) + V_{id}(m) \quad (48)$$

Where v_{id} means the velocity of the i -th particle. Also, P_{id} denotes the position of that particle in a d dimensional space for m -th iteration. The particles are accelerated by acc_1 and acc_2 towards P_{best_i} and G_{best} positions. In addition, w is the weightage with a value $\epsilon(0,1)$, and $rand_1$ and $rand_2$ are random numbers having a value between 0 to 1 [73].

The tunable parameters of the TCSC are T_2 , T_3 and k . Hence, the aim is to find the values of these parameters for which the maximum frequency deviation after a contingency (corresponding to nadir point) remains the lowest. Therefore, the objective function is given by (49).

$$OF = \Delta f(t, X) \quad (49)$$

where $\Delta f(t, X)$ denotes the maximum amount of deviation from the nominal frequency. In (49), t means time and X is composed of optimization variables, which are T_2 , T_3 and k . Thus, the optimization problem is formulated as follows.

$$\min_{X} OF(t, X) \quad (50)$$

Subject to,

$$T_2^{min} \leq T_2 \leq T_2^{max} \quad (51)$$

$$T_3^{min} \leq T_3 \leq T_3^{max} \quad (52)$$

$$k^{min} \leq k \leq k^{max} \quad (53)$$

where T_2^{min} , T_3^{min} and k^{min} are the minimum allowable values of the corresponding variables, and T_2^{max} , T_3^{max} and k^{max} are the maximum allowable values.

For executing PSO algorithm to find the optimized TCSC parameters, a joint platform of pyswarm [73] and PSS[®]E [74] is formed. PSO algorithm is developed in python and PSS[®]E command prompt is used for code execution. The proposed method is illustrated in Figure 4.3. The steps of this method are as follows.

Step-1: Model a low inertia power system in PSS[®]E. Also, initialize TCSC parameters.

Step-2: Execute dynamic simulation and record the maximum frequency deviation (i.e., frequency deviation corresponding to frequency nadir) after a large contingency.

Step-3: Provide the maximum frequency deviation as objective function in PSO algorithm.

Step-4: If the alteration in successive objective function value is less than 10^{-4} for consecutive iterations, stopping criterion is assumed to be fulfilled. Also, completion of 100 iterations is taken as another stopping criterion in this problem. Variables found from the latest iteration are the optimized TCSC parameters.

Step-5: If *step-4* is not satisfied, necessary changes in particle velocity and position are made and TCSC parameters are updated. Then, the whole process is repeated until one of the stopping criteria is satisfied.

Note that dispatch scenario of the respective system will be known beforehand. Using this market information, PSO will calculate the optimized parameters accordingly before dispatch. These optimized parameters will be subsequently utilized to set the physical parameters (i.e., L and C) of TCSC in a physical power system.

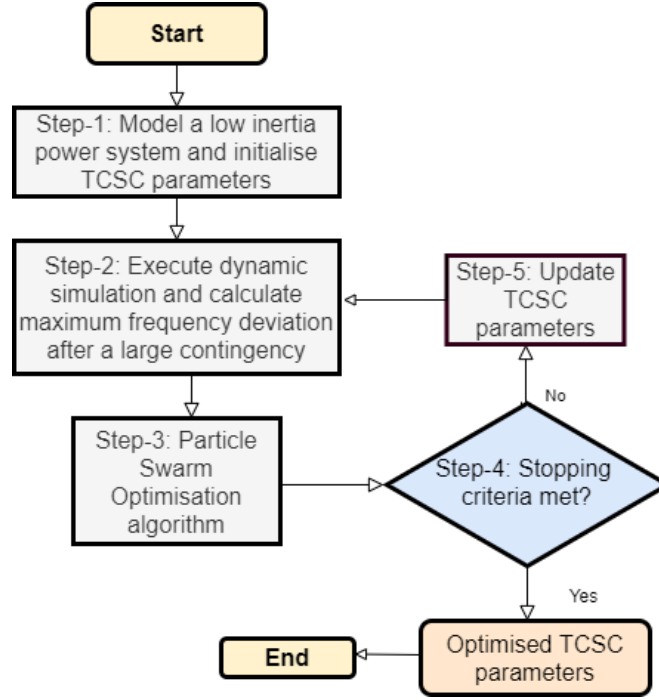


Figure 4.3: Flowchart to obtain optimised TCSC parameters

The main reason to choose Particle optimization Algorithm (PSO) for determining optimized TCSC parameters is its ability to solve complex real-world continuous non-linear problems. Since modern power systems are much more complex and larger in dimension, these attributes make PSO a convenient tool as PSO allow us to obtain high-quality solutions for these complex systems that would have been difficult to solve using Artificial neural networks or Fuzzy systems [75]. In addition, compared to traditional methods, PSO can yield better quality of solutions in shorter computing times. Also, it shows low sensitivity to noisy and missing real time data [75]. Another advantage of using PSO is, to apply PSO, the optimization problem does not need to be differentiable as is required by classical optimization methods (For example: Quasi-Newton and Gradient descent methods).

4.2.2 Enhancement of Wind Penetration Level

Wind penetration level (WPL) at any instant is defined by Eq. (54) [76].

$$WPL = \frac{P_{wind}}{P_{wind} + P_{sync} + P_{import}} \quad (54)$$

where P_{wind} is the total wind power (in MW), P_{sync} denotes the total synchronous generation (in MW) and P_{import} refers to the total interconnection import (in MW).

Maximum WPL corresponds to the highest amount of wind power that can be dispatched in a specific load condition by keeping the system frequency above a certain value following a

contingency. In this section, a mathematical relationship between frequency nadir and wind penetration level is developed. The detailed derivation is articulated below.

As discussed in chapter 3, based on the swing equation, the ROCOF (in Hz/s) following a contingency can be presented by (5) and system inertia for n number of online synchronous generators is quantified using (6).

If the change in generation is g , ΔP_g can be written as (55).

$$\Delta P_g = -g + \sum_{i=1}^{ng} \frac{f - f_o}{R} \quad (55)$$

where ng is the number of generators with active governors and R is the governor droop (in %). Furthermore, ΔP_L can be expressed by (8) as depicted in the previous chapter.

Using (55) and (8) in (6),

$$\frac{df}{dt} = \frac{f_o}{2IR} \left(k_p P_L \left(1 - \frac{f}{f_o} \right) - g + f_o \sum_{i=1}^{ng} \frac{1}{R} \left(1 - \frac{f}{f_o} \right) \right) \quad (56)$$

This provides the following expression for t .

$$t = -\frac{2IR}{k_p P_L + \left(f_o \sum_{i=1}^{ng} \frac{1}{R} \right)} \ln \left[1 - \left(1 - \frac{f}{f_o} \right) \frac{k_p P_L + \left(f_o \sum_{i=1}^{ng} \frac{1}{R} \right)}{g} \right] \quad (57)$$

Solving (57), system frequency can be expressed by (58).

$$f = f_o \left[1 - \frac{g}{\left(k_p P_L + f_o \sum_{i=1}^{ng} \frac{1}{R} \right)} \left(1 - e^{-\frac{t}{T_s}} \right) \right] \quad (58)$$

where system equivalent time constant T_s is given by (59).

$$T_s = \frac{2IR}{\left(k_p P_L + f_o \sum_{i=1}^{ng} \frac{1}{R} \right)} \quad (59)$$

Using Eq. (59) in (58), system frequency can be expressed by,

$$f = f_o \left[1 - \frac{g T_s}{2IR} \left(1 - e^{-\frac{t}{T_s}} \right) \right] \quad (60)$$

Following a contingency (generator or interconnection trip), the system frequency deviation (in p.u.) can be represented as,

$$\varphi = \left(1 - \frac{f}{f_o} \right) \quad (61)$$

Combining (60) and (61), frequency deviation is given by,

$$\varphi = -\frac{g T_s}{2IR} \left(e^{-\frac{t}{T_s}} - 1 \right) \quad (62)$$

In (62), the lowest value of $e^{-\frac{t}{T_s}}$ can be zero. When $e^{-\frac{t}{T_s}}=0$, the highest value of frequency deviation (φ_{max}) can be obtained. It is given by Eq. (63).

$$\varphi_{max} = \frac{gT_s}{2IR} \quad (63)$$

After frequency excursion, the minimum value, at which system frequency can reach i.e., frequency nadir (in Hz), can be expressed by (64).

$$f_n = f_o - \varphi_{max}f_o = f_o\left(1 - \frac{gT_s}{2IR}\right) \quad (64)$$

If the amount of synchronous generation changes, it is likely that the number of committed synchronous generators change. In other words, the amount of synchronous generation (P_{sync}) usually varies with system inertia (IR). In this paper, a linear relationship between P_{sync} and IR is assumed for simplicity, which is given by,

$$P_{sync} = bIR + c \quad (65)$$

where b is the slope and c is the constant. Note that any functional relationship can also be formed instead of (65) based on actual dispatch data in a power system. Now, the total wind power generation can be written as,

$$P_{wind} = P_L - P_{sync} - P_{import} \quad (66)$$

Using (65) and (66) in (54), WPL is given by,

$$WPL = \frac{P_L - (bIR + c) - P_{import}}{P_L} \quad (67)$$

By combining (63) and (67), WPL can be expressed by (68).

$$WPL = 1 - \frac{bgT_s}{2P_L\varphi_{max}} - \frac{c}{P_L} - \frac{P_{import}}{P_L} \quad (68)$$

Using (64) in (68) and solving, the following analytical relationship is found between f_n and WPL .

$$f_n = f_o \left[1 - \frac{bgT_s}{2P_L \left(1 - WPL - \frac{c}{P_L} - \frac{P_{import}}{P_L} \right)} \right] \quad (69)$$

To better understand (69), it is graphically illustrated in Figure 4.4 for a sample operating condition in a test network (described in the next section). For instance, a system operator chooses the lowest acceptable frequency threshold following a contingency to be 48 Hz (after allowing load shedding). From Figure 4.4, the maximum wind penetration level is around 29%. If another value is chosen as the lowest acceptable frequency threshold, the maximum WPL

would be accordingly modified. By using (69) in ‘without TCSC’ and ‘with TCSC’ cases, and comparing them, the increase in the maximum WPL can be determined.

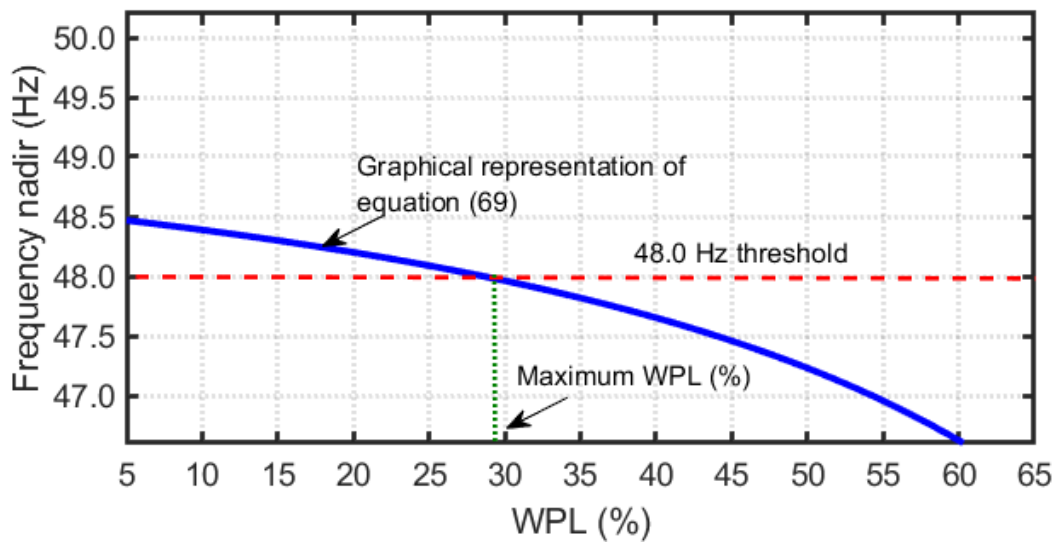


Figure 4.4: Relationship between frequency nadir and WPL

When TCSC is not active, because of cascading tripping of a large synchronous generator and interconnection, contingency size becomes larger. Consequently, frequency nadir declines (i.e., frequency deviation increases). However, when TCSC is in place, it averts network separation. Hence, contingency size reduces. As a result, frequency nadir improves. Thus, the graph shown in Figure 4.4 moves upward. It implies that more wind penetration is possible when TCSC is deployed.

4.3 Network Overview and Simulation Scenarios

4.3.1 Overview of The Low Inertia Grid

In this subsection, a test low inertia grid, similar to the one described in chapter 3 is considered to validate the efficacy of the proposed strategy. The area of interest, Area-5, as shown in Figure 4.5, is connected to its neighboring zone Area-3 via an HVAC interconnection. Area-3 is further connected to rest of the network. As discussed in the previous chapter, the test system is constructed based on South East Australian 14-Generator Model, which consists of total 5 Areas and 59 buses. In this chapter, the two major conventional power plants of Area-5 are termed as Plant-1 and Plant-2. The nameplate data of these power plants are articulated in Table 4.1. Dynamic parameters of the synchronous generators are provided in Table A-1 in the Appendix.

Table 4.1: Conventional power plant information

Power plant name	No. of generating units	Capacity of each unit (MW)	MVA rating of each unit	Inertia constant of each unit(s)
Plant-1	4	300	333.3	4.00
Plant-2	2	150	166.6	7.50

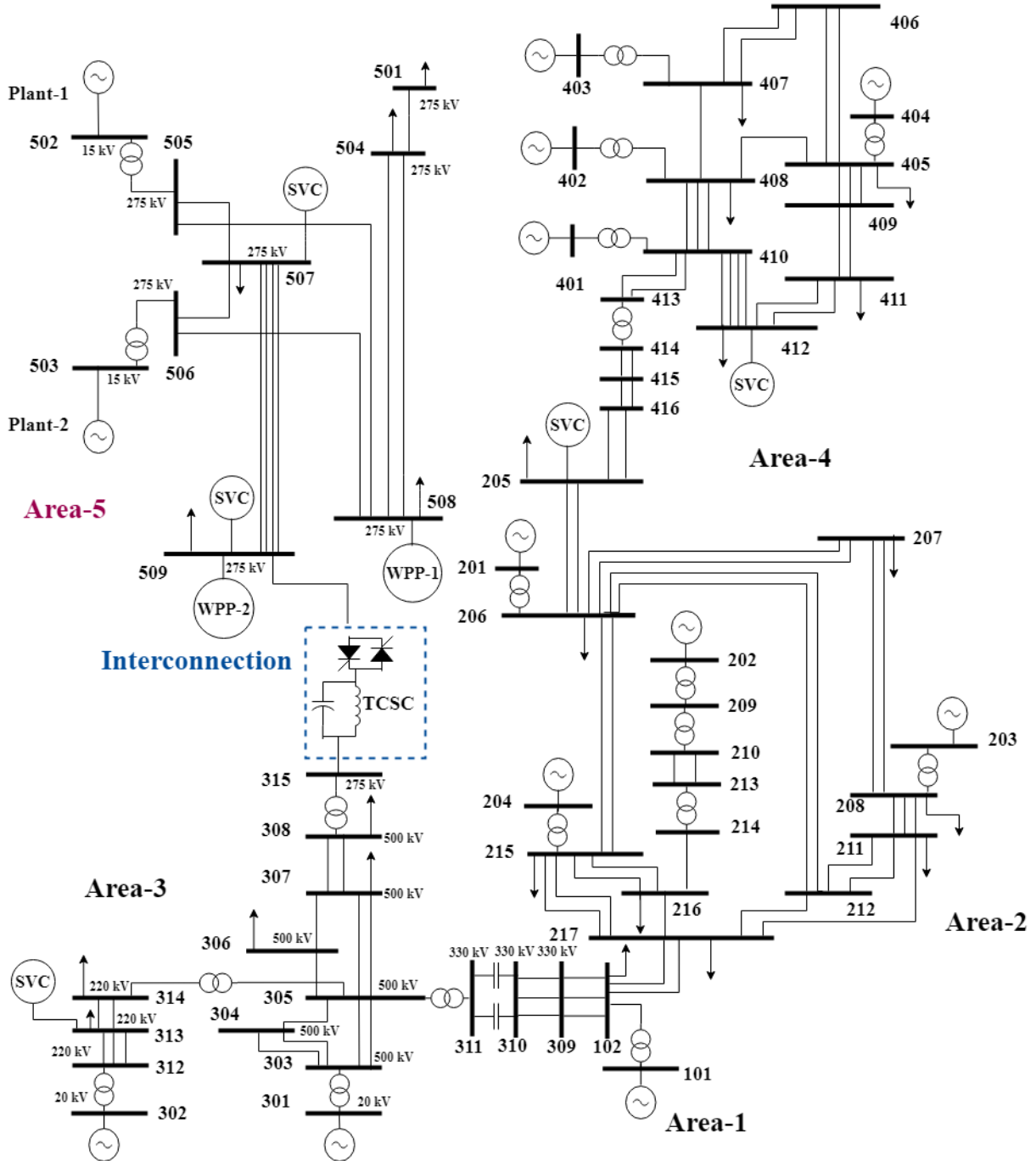


Figure 4.5: Network diagram of the simulated system

In this chapter, the amount of installed wind generation is presumed to be around 2000 MW. There are several wind power plants, which are combined in two groups, similar to the

previous chapter. Note that all the dynamic simulations are performed in PSS[®]E software, which is extensively used in power industries all over the world. Also, the network topology and generation profile are inspired from the South Australian power system, which is a typical example of a low inertia grid with prolific wind power penetration.

4.3.2 Simulation Scenarios

To validate the effectiveness of the proposed approaches in different operating conditions, two typical load scenarios are considered in this chapter. These are – (i) High load scenario, where system load is 1925 MW and (ii) Low load scenario, where system load is 1425 MW. All the investigated simulation scenarios are illustrated in Table 4.2. The number of SGs, which are committed at an instance, is varied from 5 to 3 for both load cases. Power import through interconnection is assumed to be 175 MW in all simulation cases.

Table 4.2: Simulation scenarios

Load scenario	No. of committed synchronous generator	Amount of generation from SGs (MW)	Amount of generation from WTGs (MW)	Total System Inertia (MWs)	Wind penetration level (%)
High load	5	695	1150	6584	56.93
	4	616	1250	5250	61.24
	3	531	1350	3917	65.06
Low load	5	648	650	6584	44.12
	4	558	750	5251	50.57
	3	470	850	3917	56.85

4.4 Simulation Results and Analyses

4.4.1 Optimized TCSC Parameters

Design data of TCSC, and upper and lower boundaries of TCSC parameters are respectively presented in Table A-2 and Table A-3 in the Appendix. For finding the optimized TCSC parameters, their allowable ranges are provided in the PSO algorithm. Typical ranges of these parameters are taken from [48]. The minimum values of T_2 , T_3 and k are assumed to be 0.05 s, 0.3 s and 0.5 respectively. The maximum values of these parameters are presumed to be 0.2 s, 1 s and 30 respectively. The optimal TCSC parameters will be determined and

implemented before the real-time operation by considering the maximum size of probable contingency (i.e. worst-case scenario). Since these optimized parameters are determined for the worst-case scenario, they are likely to be applicable to the other less severe contingency cases.

To ensure global solution, PSO algorithm is executed several times until the optimization outputs start to repeat. These outputs are then used to calculate the objective function. The values of the optimization variables, which yield the minimum objective function, are eventually taken as the optimized TCSC parameters. Table 4.3 shows the final results. These values are accordingly used in TCSC design.

Table 4.3: Optimised TCSC parameters

Load Scenario	No. of committed synchronous generators	T ₂ (s)	T ₃ (s)	k
High load	5	0.1507	0.6685	8.5441
	4	0.1801	0.3010	7.5608
	3	0.1730	0.5200	10.4103
Low load	5	0.1549	0.7787	24.5500
	4	0.1368	0.8961	8.4788
	3	0.1068	0.3748	9.2102

4.4.2 Frequency Response in High Load Scenario

The frequency dependent model demonstrated in Section 4.2 and the obtained optimal parameters of the TCSC shown in Table 4.3 are utilized in this section to avoid network separation. System frequency is calculated using the concept of Centre of Frequency (CoF) as described in chapter 3.

Note that the low inertia part of the considered grid, i.e., Area-5 resembles the equivalent high voltage transmission network of South Australian power system. As such, the grid code of Australian National Electricity Market is considered as the standard. According to this grid code, the tolerance band of normal operating frequency is 49 Hz - 51 Hz and extreme frequency excursion tolerance limits are 47 Hz - 52 Hz [78]. Accordingly, UFLS is initiated when system frequency goes below 49 Hz. Likewise, system experiences a blackout when the frequency goes below 47 Hz. Note that the UFLS model relies on the number of stages available in the load shedding process. Assume that m_1 , m_2 and m_3 percent of load is shed in three stages. Therefore, the total load is multiplied by Eq. (70) while load shedding is applied.

$$\frac{(1 - m_1\%)}{100} \quad : \text{1st stage, } f < f_{TH1}$$

$$\frac{(1 - m_1\% - m_2\%)}{1 - m_1\%} : 2nd\ stage, f < f_{TH2} \quad (70)$$

$$\frac{(1 - m_1\% - m_2\% - m_3\%)}{1 - m_1\% - m_2\%} : 3rd\ stage, f < f_{TH3}$$

where f_{TH1} , f_{TH2} and f_{TH3} indicate the frequency thresholds (in Hz) to activate the 1st stage, 2nd stage and 3rd stage of load shedding respectively.

In high load condition, 300 MW synchronous generation trip is applied for all cases. Figure 4.6 depicts overall system performance when 5 synchronous machines are available in Area-5. Following the loss of 300 MW generator, the interconnection intends to draw more power from the adjacent generation rich area. Eventually, the power flow through the interconnection crosses the maximum power carrying capability of the line. As a result, the interconnection trips due to loss of synchronism as shown in Figure 4.6(d). Due to this cascading contingency, the frequency decreases and eventually falls below 47 Hz. Consequently, all the generators in Area-5 get disconnected. It is worth mentioning that when the system frequency drops below 49 Hz, the UFLS scheme given by (70) is activated. However, even after three stages of load cut, the frequency excursion does not stop. Eventually, system undergoes blackout if TCSC is not utilized as shown in Figure 4.6(a) (Blue trace). When the frequency reduces, the TCSC operation is enabled if proposed technique is undertaken. Consequently, the total reactance of the interconnection decreases as shown in Figure 4.6(b). It essentially increases the maximum power transfer capability. As a result, interconnection power flow does not cross the maximum limit as shown in Figure 4.6(c). The maximum power flow through the interconnection is found to be 458 MW from Figure 4.6(c). Accordingly, the network separation is prevented. It is noticed from Figure 4.6(a) (Red trace) that the frequency nadir for this case is 48.45 Hz. Therefore, the possibility of blackout is mitigated by incorporating TCSC with the interconnection for 5 machines case.

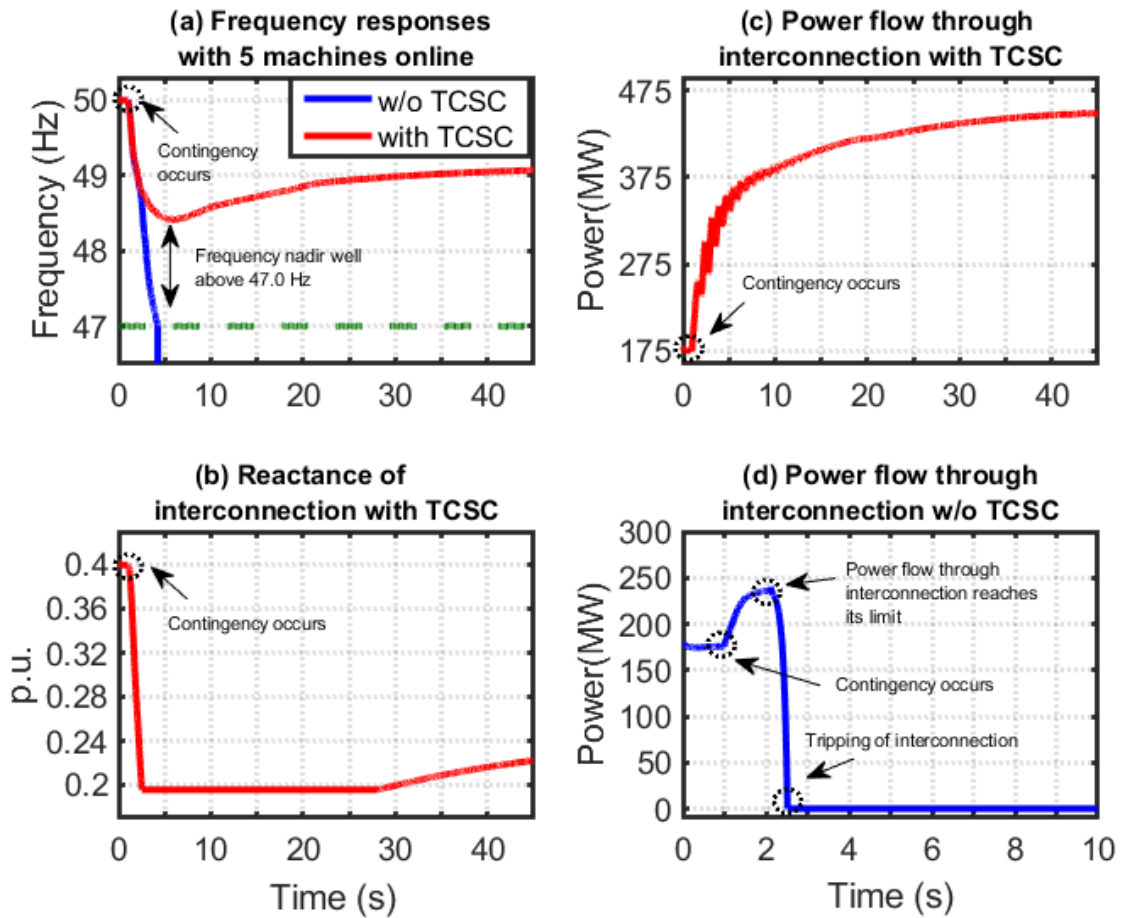


Figure 4.6: System performance for 5 machines case in high load scenario

Before the interconnection trip due to loss of synchronism, the Area-5 along with its adjacent areas constitutes a synchronous system. Therefore, before the interconnection trip, the frequency responses of Area-5 and Area-3 are the same. However, after the interconnection trip, Area-3 encounters over-generation. As a result, the frequency starts to increase and goes above 50 Hz.

Following the interconnection trip, Area-3 is still synchronously connected to Area-1, Area-2 and Area-4. In this whole network, numerous synchronous generators are committed. Therefore, the inertia and governor responsive reserve are high. Eventually, the frequency of Area-3 is arrested at 50.2 Hz. Later on, the frequency starts to decrease and settles down close to the nominal value. Figure 4.7 depicts the frequency response of Area-3 after the interconnection trip.

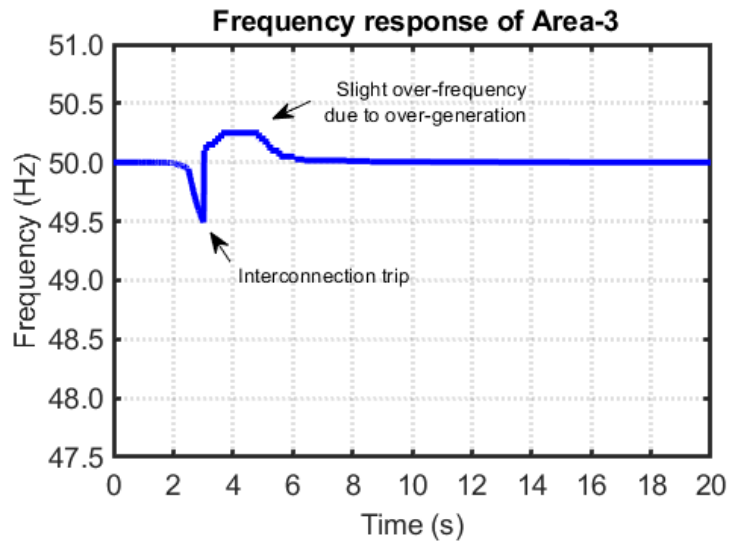


Figure 4.7: Frequency response of Area-3 for 5 machines case in high load scenario

The simulated grid undergoes system-wide blackout for 4 machines and 3 machines case as well when TCSC is not in action. However, after TCSC incorporation, frequency nadirs are found to be 48.13 Hz and 48.05 Hz for 4 machines and 3 machines cases as shown in Figure 4.8(a) and Figure 4.8(b) respectively. Variation of line reactance and power flow through interconnection are not shown for these two cases as they are identical as that of 5 machines case. It is to be clarified that in Figure 4.8, for both 4 machines and 3 machines case, when TCSC is not incorporated, UFLS is activated and 30% of the total load is shed. In these cases, system inertia and governor responsive reserve are low. Also, due to the network separation, the contingency size becomes large. As a result, even after substantial load cut, the system frequency drops below 47 Hz. Consequently, the system encounters blackout when TCSC is not incorporated.

Utilizing (70), the amounts of load shedding after utilizing TCSC are found to be 94 MW, 103 MW, 111 MW in 5 machines, 4 machines and 3 machines case respectively. Therefore, it is revealed that in high load case, the frequency responsive TCSC averts network separation and blackout. However, the system faces reasonable quantities of load shedding.

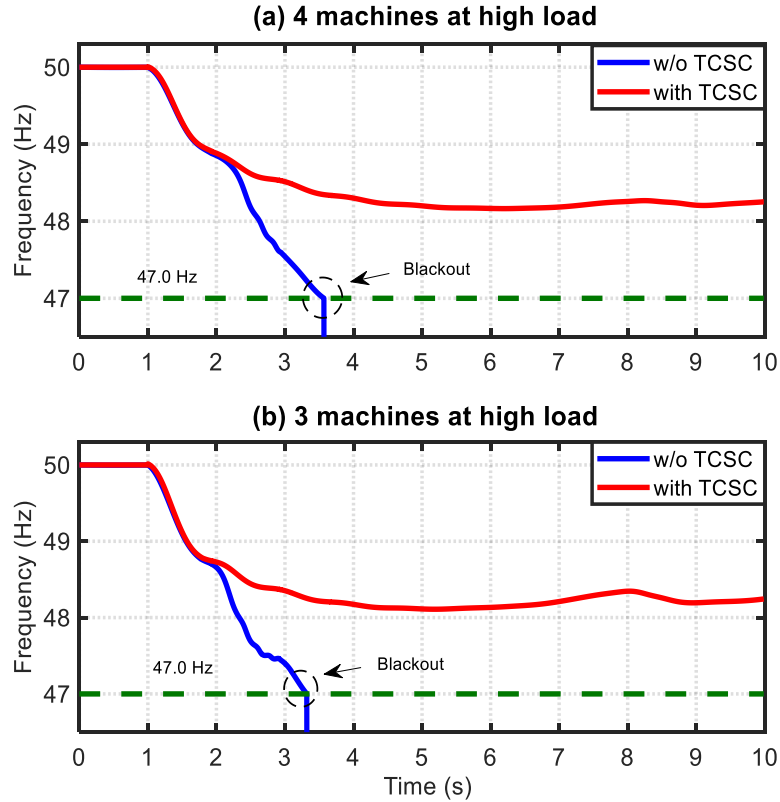


Figure 4.8: System performance for 4 machines case and 3 machines case in high load scenario

4.4.3 Frequency Response in Low Load Scenario

In this scenario, the same contingency as of high load case is applied. Without TCSC, the interconnection trips due to loss of synchronism. As a result, the system incurs blackouts in all cases. Figure 4.9 depicts the frequency response curves.

When TCSC is connected, network separation is averted. As such, system frequency is rescued after applying reasonable amounts of load shedding. The frequency nadirs become 48.08 Hz, 48 Hz and 47.95 Hz in 5 machines, 4 machines and 3 machines cases respectively. Hence, the frequency response is more vulnerable in low load scenario compared to high load scenario. The corresponding load shedding amounts are found to be 134 MW, 143 MW and 154 MW using (70). Therefore, the system wide blackout can be stopped by using the frequency responsive TCSC.

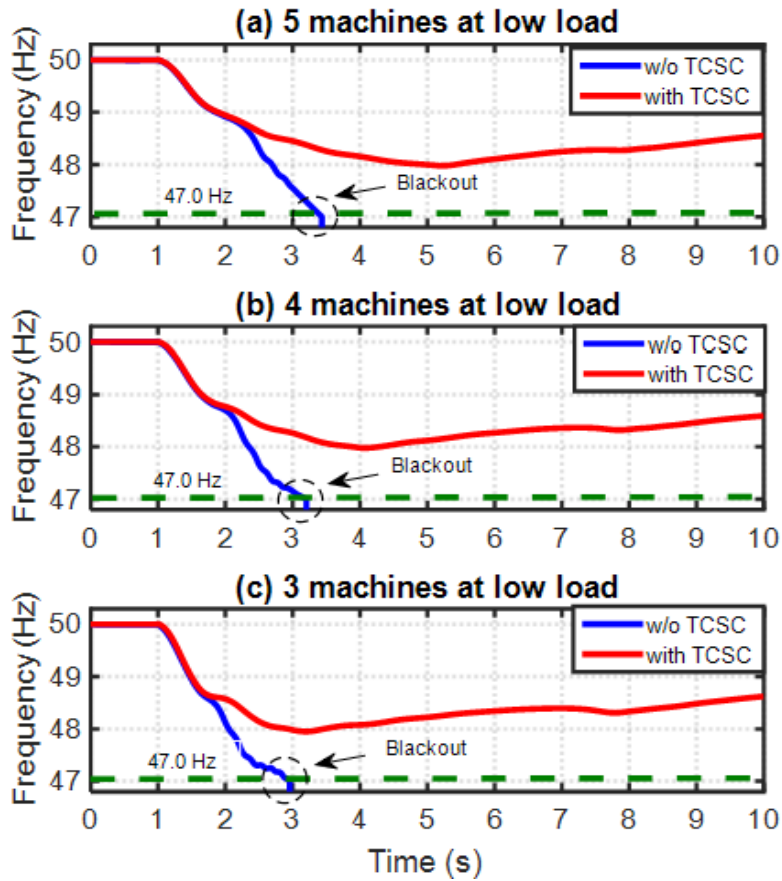


Figure 4.9: Frequency response for low load scenario

4.4.4 Performance Comparison with An Existing Technique

To compare the obtained results with existing technology for preventing network separation i.e., FSC, two scenarios are considered: i) 100 MW contingency ii) 300 MW contingency. It is assumed that 5 machines are present in the system and system load is 1925 MW. For both cases, FSC is designed to provide 20% compensation. On the contrary, compensation level can be varied from 0% to 50% by TCSC incorporation. The obtained results for both scenarios are as follows:

4.4.4.1 100 MW Contingency

In this scenario, it is assumed that a generator of 100 MW capacity has tripped. If no compensation is provided, network separation takes place and system encounters blackout. However, if the FSC comes into action and provides 20% compensation, the power carrying capability of the interconnection increases. As a result, network separation is avoided and frequency excursion reaches 49.21 Hz according to Figure 4.10 (Green trace). If TCSC is incorporated instead of FSC, again network separation is circumvented and system does not undergo blackout. Frequency nadir is found to be 49.22 Hz according to Figure 4.10 (Red

trace). Thus, FSC and TCSC perform almost identically in this scenario and prevent system-wide blackout.

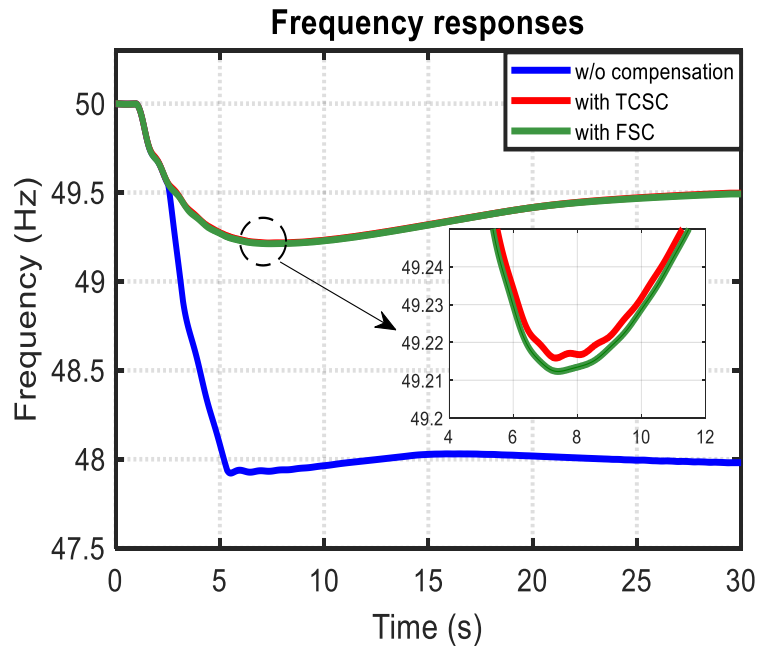


Figure 4.10: Frequency response comparison with existing technique for 100 MW contingency

4.4.4.2 300 MW Contingency

In this scenario, the typical case of 300 MW generator trip is considered. Note that FSC is supposed to provide 20% compensation as its compensation level is not changeable. Higher compensation level is also not acceptable for FSC as it would increase the risk of Sub-Synchronous Resonance (SSR). On the contrary, as TCSC is supposed to provide a variable compensation level depending on the contingency size, it will provide a higher compensation in this scenario than the previous one. Simulation results show that system undergoes blackout when no compensation scheme is undertaken. Also, FSC incorporation fails to prevent network separation and system-wide blackout as shown in Figure 4.11. However, TCSC incorporation results in a frequency nadir of 48.25 Hz, and risk of blackout are averted. Thus, even though FSC performs adequately in case of small contingencies, it fails to avert the risk of blackout in case of larger contingencies.

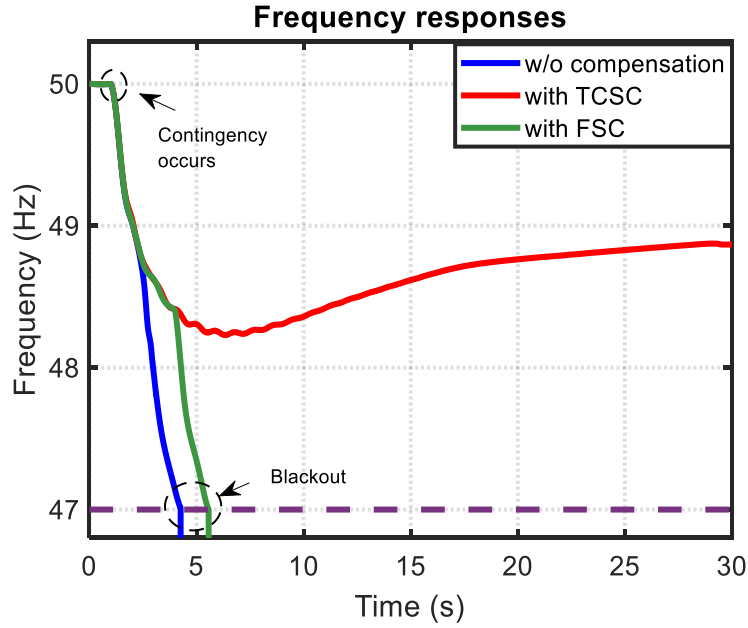


Figure 4.11: Frequency response comparison with existing technique for 300 MW contingency

4.4.5 Improvement of Maximum Wind Penetration Level

To estimate the improvement of the maximum wind penetration level after compensating the interconnection via TCSC, the analytical expression of (69) is applied. In (69), the contingency size depends on whether the TCSC is in place. Note that before connecting TCSC, cascading contingency takes place. A trip of 300 MW synchronous generation causes the interconnection to reach its maximum limit of around 240 MW. Thus, the total contingency size becomes 540 MW. If a FSC of 20% compensation level is considered, it is found that for around 180 MW generator trip, the enhancement of the power carrying capability of the interconnection by FSC becomes inadequate. As a result, the overall contingency level becomes 420 MW when FSC is utilized instead of TCSC. Note that for a 300 MW generation loss, the FSC fails to prevent network separation and subsequent blackout. Thus, there exist no visible difference in maximum wind penetration level for FSC utilization and no TCSC incorporation. However, when TCSC is connected, the interconnection does not trip following the loss of 300 MW synchronous generation. Therefore, the contingency size remains 300 MW. Figure 4.12(a) depicts the plot between frequency nadir and WPL in 5 machines case under high load scenario. Without TCSC, the maximum WPL is estimated as 29.4% by assuming the lowest acceptable frequency threshold to be 48 Hz. When FSC is utilized, the maximum WPL is found to be 42.5%. On the contrary, when TCSC is utilized, the maximum WPL becomes 58.8%. It is to be clarified that in this paper, “without TCSC” refers to without any

compensation, “with FSC” means with only FSC, “with TCSC” means with only TCSC and maximum WPL enhancement means difference in maximum WPL when TCSC is in place and when no compensation is utilized.

Similarly, Figure 4.12(b) graphically illustrates the relationship between frequency nadir and WPL in 5 machines case under low load scenario. Before connecting TCSC, the maximum WPL is found to be 20.4%. When FSC is utilized, the maximum WPL is found to be 32.1%. However, it rises to 50.7% when the interconnection is compensated by TCSC. Notably, after deploying TCSC, the maximum WPL improves by 29.4% and 30.3% in 5 machines case during high load and low load scenarios respectively.

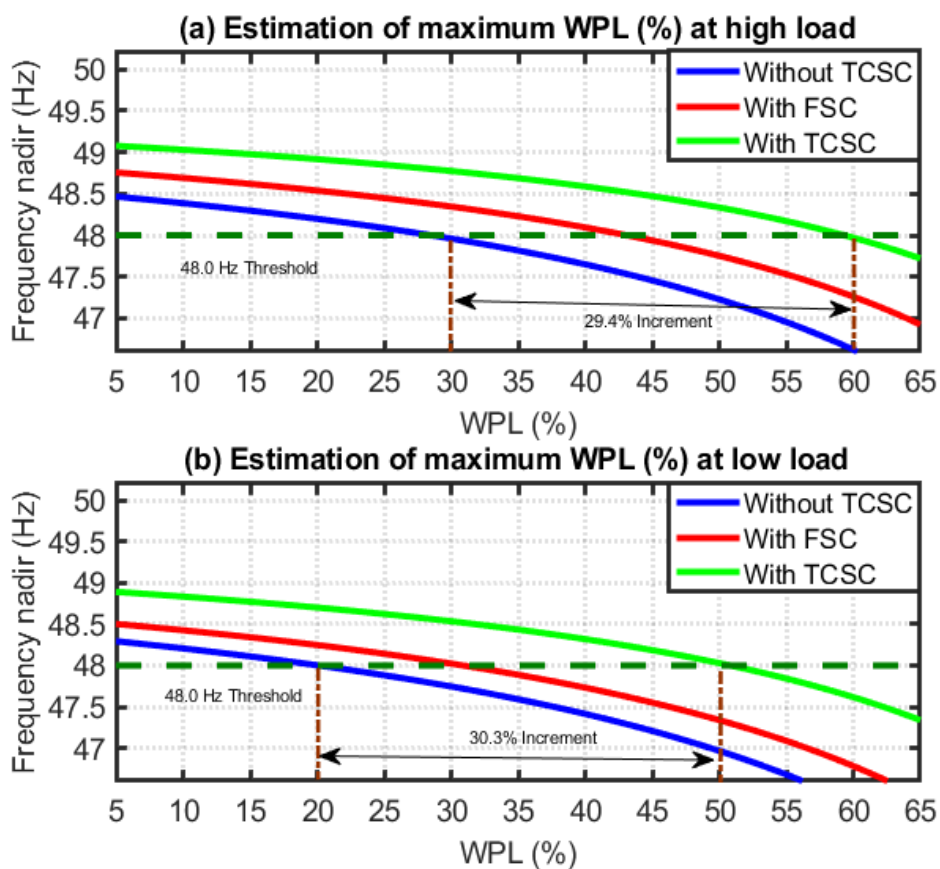


Figure 4.12: Maximum WPL without and with TCSC in 5 machines case (a) High load scenario (b) Low load scenario

Table 4.4 enumerates the maximum WPL in different operating scenarios. It can be seen that the maximum WPL improves by 29.4% to 31.3% in various cases. Therefore, significant increase in wind penetration level is achieved when TCSC is used to compensate the interconnection.

In addition, from Table 4.4, the maximum WPL without TCSC varies from 29.4% to 40% in high load condition. Referring to Table 4.2, WPL in this scenario is 56.93% to 65.06%.

Noticeably, these values are higher than the maximum permissible limits. The same remark can be drawn for low load scenario as well. Essentially, these high WPLs lead to system wide blackout. It basically indicates the need of compensating the interconnection via TCSC to improve frequency resilience and wind penetration level.

Table 4.4: Enhancement in Maximum WPL

Load scenario	No. of committed synchronous generators	Maximum WPL without TCSC (%)	Maximum WPL With FSC (%)	Maximum WPL with TCSC (%)	Increase in maximum WPL (%)
High load	5	29.4	42.5	58.8	29.4
	4	35.9	49.8	65.8	29.9
	3	40.0	54.2	70.1	30.1
Low load	5	20.4	32.1	50.7	30.3
	4	24.1	37.2	55.1	31.0
	3	29.7	42.8	61.0	31.3

4.5 Further Discussions

In this thesis, two different types of frequency control strategies are explored. The first one is frequency control via Energy Storage Systems (ESS), which is a frequency control technique from the load perspective. Another one is controlling system frequency via TCSC where TCSC controls the power import for the adjacent area. Thus, it can be considered as a frequency control technique from generation perspective. To compare between this two techniques when they are applied in a low inertia grid, a detailed investigation is carried out in this subsection. Here, 300 MW generator trip is considered as the contingency for comparing the system performance where the number of synchronous generators is varied from 4 to 3. For both of the scenarios, it is assumed that system load is 1425 MW (Low load scenario) and interconnection import is 175 MW. In this subsection, “With ESS” means that only the Energy Storage System (Consisting of SMES and BESS) is incorporated and “With TCSC” denotes that only TCSC is being utilized.

When there are 4 synchronous machines are online, without TCSC or ESS, network separation occurs and system encounters blackout. When there is only ESS present in the system, following the contingency, network separation cannot be avoided. However, due to additional active power support from SMES and BESS, the system manages to escape blackout. The ROCOF and frequency nadir are found to be 1.39 Hz/s and 47.52 Hz respectively. On the contrary, when TCSC is incorporated, network separation is avoided. Subsequently, blackout is also mitigated. The ROCOF and frequency nadir are found to be 0.52 Hz/s and 48.00 Hz

respectively for this scenario. Note that although ESS can avert blackout, it yields very high ROCOF and inferior system frequency response than that of with TCSC.

Furthermore, when 3 synchronous generators are committed, the system inertia is relatively low. Thus, without TCSC or ESS, the system encounters network separation and subsequent blackout. When ESS is incorporated to provide additional active power support, after considerable load shedding, it averts the risk of blackout. The ROCOF and frequency nadir are found to be 1.87 Hz/s and 47.05 Hz respectively. However, when TCSC is being incorporated, the frequency nadir is 47.95 Hz and system ROCOF is 0.78 Hz/s. Thus, again TCSC incorporation yields relatively superior system frequency response compared to that of with ESS.

Therefore, it can be deduced from this aforementioned investigation that frequency control via generation perspective yields a better system frequency compared to frequency control techniques via load perspective in general.

Table 4.5: Comparison of system frequency response

No. of online synchronous generators	Contingency size (MW)	ROCOF magnitude (Hz/s)			Frequency nadir (Hz)		
		Without ESS or TCSC	With ESS	With TCSC	Without ESS or TCSC	With ESS	With TCSC
4	300	2.59	1.39	0.52	Blackout	47.52	48.00
3	300	3.06	1.87	0.78	Blackout	47.05	47.95

4.6 Summary

This chapter comprehensively investigates the utilization of frequency responsive TCSC to enhance frequency resilience and wind penetration level in a low inertia interconnected power system. To this end, at first, optimal TCSC parameters are determined using PSO algorithm. Afterwards, TCSC is incorporated with the target of avoiding network separation and the risk of cascaded contingency.

Without TCSC, after the loss of a large synchronous generator, the interconnection reaches its maximum limit and subsequently trips due to loss of synchronism. Consequently, the low inertia system has to rely on its own primary frequency control capability and UFLS to stop the frequency excursion. However, due to huge contingency size, the frequency drops below 47 Hz, and the network encounters a blackout. It is revealed that the frequency

responsive TCSC successfully compensates the interconnection and increases the power transfer limit. Therefore, the network separation is prevented and the frequency is rescued after deploying the frequency responsive TCSC in all simulation cases. In high load condition, frequency nadirs become 48.45 Hz, 48.13 Hz and 48.05 Hz in 5 machines, 4 machines and 3 machines cases respectively. The corresponding load shedding amounts are found to be 94 MW, 103 MW, 111 MW. Furthermore, during low load condition, the frequency nadirs are 48.08 Hz, 48 Hz and 47.95 Hz in 5 machines, 4 machines and 3 machines cases respectively. Also, the corresponding load shedding quantities are 134 MW, 143 MW and 154 MW. Hence, the frequency response is more vulnerable and the system incurs higher amount of load cut in low load scenario. It is revealed that the proposed technique yields superior system performance than that of existing technology (i.e., fixed series capacitors).

In addition, an analytical tool is developed to determine the increase in wind power penetration level. It is demonstrated that wind penetration level (WPL) increase substantially after embedding the TCSC in the interconnection. Using the analytical expression, it is found that for high load case, the maximum WPL enhances by 29.4%, 29.9% and 30.1% in various operating conditions. Subsequently, it is noticed that enhancement in maximum WPL are 30.3%, 31% and 31.3% for different machine case in low load condition. Therefore, the deployment of frequency responsive TCSC not only improves the frequency resilience but also allows more wind resources to be integrated in a low inertia network.

At the last part of this subsection, a comparative analysis is done to determine which one among frequency control technique via load perspective and generation perspective yields superior system performance. Simulation results show that frequency control from generation perspective yields a superior grid frequency response than that of from load perspective.

Chapter 5

Conclusions and Recommendation for Future Research

5.1 Conclusion

Wind-dominated power systems may suffer from inadequate system inertia due to retirement of conventional fossil-fuel driven synchronous generators. Extensive analyses were carried out in chapter 3 to investigate the utilization of ESS in frequency response improvement of low inertia systems. To this end, a mathematical framework of determining minimum sizes of SMES and BESS was developed and an operational strategy for these ESS was outlined. The major findings of this portion of the thesis are summarized as follows.

- i. The ratings of SMES and BESS were assessed considering 3 online synchronous machines while the interconnection tripping size was 200 MW.
- ii. For 200 MW contingency, the minimum SMES and BESS ratings were found to be approximately 47 MW and 97 MW respectively to keep ROCOF and frequency deviation within the given acceptable limits.
- iii. Frequency response performances were analyzed in four different case studies following the loss of interconnection. It was found that when ESS are activated, ROCOF was confined to the maximum allowable limit of 1 Hz/s. Furthermore, the frequency nadirs were above 49 Hz (in 200 MW contingency) or very close to 49 Hz (in 300 MW contingency). Consequently, load shedding was either fully averted or significantly minimized.
- iv. Although the ROCOF showed an improving trend due to additional inertial support when synchronous condenser (SC) is placed instead of ESS, in three case studies, SC failed to keep ROCOF below the safety threshold. In addition, inclusion of SC did not reduce the amount of load shedding in any case study.
- v. When only BESS was incorporated, it yielded slightly inferior system performance than that of the proposed methodology.
- vi. Therefore, it was revealed that the proposed methodology yields adequate frequency response to make a low inertia grid more secure and resilient.

It is already discussed that when the system inertia is insufficient, a large contingency in the power importing zone may overload an AC interconnection. Consequently, the

interconnection could trip due to loss of synchronism, which may lead to system-wide blackout. In this thesis, frequency responsive TCSC was utilized in this respect. Furthermore, an analytical method of determining maximum wind penetration level was proposed. The key findings of this portion are summarized as follows.

- i. Firstly, optimal TCSC parameters were determined using PSO algorithm. Afterwards, TCSC was incorporated with the target of avoiding network separation and the risk of cascaded contingency.
- ii. Without TCSC, after the loss of a large synchronous generator, the interconnection reached its maximum limit and subsequently tripped due to loss of synchronism. Due to huge contingency size, the frequency dropped below 47 Hz, and the network encountered a blackout.
- iii. The frequency responsive TCSC successfully compensated the interconnection and increased the power transfer limit. Therefore, the network separation was prevented and the frequency was rescued after deploying the frequency responsive TCSC in all simulation cases.
- iv. The frequency response was more vulnerable and the system incurred higher amount of load cut in low load scenario than that of high load scenario.
- v. It was revealed that the proposed technique yielded superior system performance than that of existing technology (i.e., fixed series capacitors).
- vi. It was demonstrated that wind penetration level (WPL) increased substantially after embedding the TCSC in the interconnection.
- vii. Therefore, it can be concluded that the deployment of frequency responsive TCSC not only improved the frequency resilience but also allowed more wind resources to be integrated in a low inertia network.

5.2 Recommendations for Future Works

The following scopes can be recommended for future researchers and engineers.

- i. A comparative analysis among the results obtained by the proposed sizing methodology and an optimal sizing algorithm using any heuristic method can be carried out in the future.
- ii. A techno-economic analysis of incorporating frequency responsive TCSC can be performed in future. Such an analysis can provide important insights on the affordability of this solution.

- iii. The combination of zonal inertia constrained dispatch and frequency responsive TCSC can further enhance the frequency resilience of renewable rich networks. Such an approach can be investigated in future.
- iv. Other FACTS devices such as Unified Power Flow Controller (UPFC) and Energy Storage Systems (ESS) can be deployed for averting the risk of network separation in renewable prolific power systems. Performance comparison and value proposition of various solutions can be of great interest and can be investigated in future.
- v. Enhancement of wind penetration level can be determined using heuristic optimization algorithms under certain constraints. As such, analytical method presented in this paper can be validated against the optimal solution in future works.

References

- [1] R. Rajan, F. M. Fernandez, and Y. Yang, “Primary frequency control techniques for large-scale PV-integrated power systems: A review,” *Renewable and Sustainable Energy Reviews*, vol. 144. Elsevier Ltd, Jul. 01, 2021.
- [2] D. Drysdale, B. V. Mathiesen, and S. Paardekooper, “Transitioning to a 100% renewable energy system in Denmark by 2050: assessing the impact from expanding the building stock at the same time,” *Energy Efficiency*, vol. 12, no. 1, pp. 37–55, Mar. 2018.
- [3] R. J. Batterham, “Clean power technology,” *Engineering*, vol. 6, no. 12, pp. 1349–1350, Dec. 2020.
- [4] “Global energy transformation: A roadmap to 2050 (2019 edition),” 2019.[Online] Available: <https://www.irena.org/publications/2019/Apr/Global-energy-transformation-A-roadmap-to-2050-2019Edition#:~:text=Increased%20use%20of%20renewable%20energy,key%20climate%20goals%20by%202050>. [Accessed Jul. 19, 2021].
- [5] J. Liu, Q. Wang, Z. Song, and F. Fang, “Bottlenecks and countermeasures of high-penetration renewable energy development in China,” *Engineering*, Dec. 2020.
- [6] "Global Wind Report 2019," Global Wind Energy Council (GWEC), 2019. [Online]. Available: <https://gwec.net/global-wind-report-2019/>. [Accessed March 2020].
- [7] J. Ekanayake and N. Jenkins, “Comparison of the response of doubly fed and fixed-speed induction generator wind turbines to changes in network frequency,” *IEEE Trans. Energy Conversion*, vol. 19, no. 4, pp. 800–802, Dec. 2004.
- [8] C. Medina, C.R.M. Ana, and G. González, G., “Transmission grids to foster high penetration of large-scale variable renewable energy sources—a review of challenges, problems, and solutions,” *International Journal of Renewable Energy Research (IJRER)*, 12(1), pp.146-169, 2022.
- [9] M. Leslie, “Transmission infrastructure challenges use of renewable energy,” *Engineering*, vol. 6, no. 6, pp. 587–589, Jun. 2020.
- [10] T. Kerdphol, F. S. Rahman, M. Watanabe, Y. Mitani, D. Turschner and H. Beck, "Enhanced virtual inertia control based on derivative technique to emulate simultaneous inertia and damping properties for microgrid frequency regulation," *IEEE Access*, vol. 7, pp. 14422-14433, 2019.

- [11] Yan, R., Saha, T.K., Modi, N., Masood, N.A. and Mosadeghy, M., “The combined effects of high penetration of wind and PV on power system frequency response”, *Applied Energy*, vol.145, pp.320-330, 2015.
- [12] H. Gu, R. Yan, T. K. Saha, E. Muljadi, J. Tan and Y. Zhang, "Zonal inertia constrained generator dispatch considering load frequency relief," *IEEE Trans. Power Systems*, vol. 35, no. 4, pp. 3065 – 3077, 2020.
- [13] DNV KEMA Energy & Sustainability. "RoCoF an independent analysis on the ability of generators to ride through rate of change of frequency values up to 2Hz/s", Available:
http://www.eirgridgroup.com/sitefiles/library/EirGrid/DNV_KEMA_Report_RoCoF_20130208final_.pdf. [Accessed: 10-Feb.-2021].
- [14] Yan, R., Saha, T.K., N.A. Masood, Bai, F. and Gu, H., “The anatomy of the 2016 South Australia blackout: a catastrophic event in a high renewable network”, *IEEE Trans. Power Systems*, vol. 33, no. 5, pp.5374-5388, 2018.
- [15] De Boeck, S. and Van Hertem, D., “Under frequency load shedding schemes in systems with high PV penetration: Impact and improvements”, in Proc. *2015 IEEE Eindhoven PowerTech*, pp. 1-6, 2015.
- [16] N. Masood, R. Yan, T. K. Saha and S. Bartlett, "Post-retirement utilisation of synchronous generators to enhance security performances in a wind dominated power system," *IET Generation, Transmission & Distribution*, vol. 10, no. 13, pp. 3314-3321, 2016.
- [17] Nguyen, H.T., Yang, G., Nielsen, A.H. and Jensen, P.H. “Combination of synchronous condenser and synthetic inertia for frequency stability enhancement in low-inertia systems”, *IEEE Trans. Sustainable Energy*, vol. 10, no. 3, pp.997-1005, 2018.
- [18] X. Zeng, T. Liu, S. Wang, Y. Dong and Z. Chen, "Comprehensive coordinated control strategy of PMSG-based wind turbine for providing frequency regulation services," *IEEE Access*, vol. 7, pp. 63944-63953, 2019.
- [19] I. Sami, N. Ullah, S. M. Muyeen, K. Techato, M. S. Chowdhury and J. -S. Ro, "Control methods for standalone and grid connected micro-hydro power plants with synthetic inertia frequency support: s comprehensive review," *IEEE Access*, vol. 8, pp. 176313-176329, 2020.
- [20] Tenfen, Daniel, Erlon C. Finardi, Benoit Delinchant, and Frederic Wurtz. "Lithium-ion battery modelling for the energy management problem of microgrids." *IET Generation, Transmission & Distribution*, vol. 10, no. 3, pp. 576-584, 2016.

- [21] A. Saleh, A. Awad and W. Ghanem, "Modeling, control, and simulation of a new topology of flywheel energy storage systems in microgrids," *IEEE Access*, vol. 7, pp. 160363-160376, 2019.
- [22] R. K. Sarojini and P. Kaliannan, "Inertia Emulation Through Supercapacitor for a Weak Grid," *IEEE Access*, vol. 9, pp. 30793-30802, 2021.
- [23] X. Lin and Y. Lei, "Coordinated Control Strategies for SMES-Battery Hybrid Energy Storage Systems," *IEEE Access*, vol. 5, pp. 23452-23465, 2017.
- [24] Farhadi, M. and Mohammed, O., "Energy storage technologies for high-power applications", *IEEE Trans. Industry Applications*, vol. 52, no. 3, pp.1953-1961, 2015.
- [25] Delille, G., Francois, B. and Malarange, G., "Dynamic frequency control support by energy storage to reduce the impact of wind and solar generation on isolated power system's inertia", *IEEE Trans. Sustainable Energy*, vol. 3, no. 4, pp.931-939, 2012.
- [26] Oudalov, A., Chartouni, D. and Ohler, C., "Optimizing a battery energy storage system for primary frequency control". *IEEE Trans. Power Systems*, vol. 22, no. 3, pp.1259-1266, 2007.
- [27] H. Xie, X. Teng, Y. Xu and Y. Wang, "Optimal energy storage sizing for networked microgrids considering reliability and resilience," *IEEE Access*, vol. 7, pp. 86336-86348, 2019.
- [28] A. Headley and D. Copp, "Energy storage sizing for grid compatibility of intermittent renewable resources: A California case study", *Energy*, vol. 198, p. 117310, 2020.
- [29] U. T. Salman, F. S. Al-Ismail and M. Khalid, "Optimal sizing of battery energy storage for grid-connected and isolated wind-penetrated microgrid," *IEEE Access*, vol. 8, pp. 91129-91138, 2020.
- [30] M. Li, L. Wang, Y. Wang and Z. Chen, "Sizing optimization and energy management strategy for hybrid energy storage system using multi-objective optimization and random forests," *IEEE Transaction on Power Electronics*, vol. 36, no. 10, pp. 11421-11430, Oct. 2021.
- [31] V. Knap, S. K. Chaudhary, D. Stroe, M. Swierczynski, B. Craciun and R. Teodorescu, "Sizing of an energy storage system for grid inertial response and primary frequency reserve," *IEEE Transaction on Power Systems*, vol. 31, no. 5, pp. 3447-3456, Sept. 2016.
- [32] E. Spahic, D. Varma, G. Beck, G. Kuhn and V. Hild, "Impact of reduced system inertia on stable power system operation and an overview of possible solutions", In Proc.

- IEEE Power and Energy Society General Meeting (PESGM)*, Boston, MA, 2016, pp. 1-5, 2016.
- [33] M. Ramírez, R. Castellanos, G. Calderón, and O. Malik, "Placement and sizing of battery energy storage for primary frequency control in an isolated section of the Mexican power system", *Electric Power Systems Research*, vol. 160, pp.142-150, 2018.
- [34] F. Zhu, X. Zhou, Y. Zhang, D. Xu and J. Fu, "A load frequency control strategy based on disturbance reconstruction for multi-area interconnected power system with hybrid energy storage system", *Energy Reports*, vol. 7, pp. 8849-8857, 2021.
- [35] H. Shayeghi, A. Rahnama and H. Alhelou, "Frequency control of fully-renewable interconnected microgrid using fuzzy cascade controller with demand response program considering", *Energy Reports*, vol. 7, pp. 6077-6094, 2021.
- [36] Q. Meng, Y. Li, X. Ren, C. Xiong, W. Wang and J. You, "A demand-response method to balance electric power-grids via HVAC systems using active energy-storage: Simulation and on-site experiment", *Energy Reports*, vol. 7, pp. 762-777, 2021.
- [37] H. Gu, R. Yan, T. K. Saha, E. Muljadi, J. Tan and Y. Zhang, "Zonal inertia constrained generator dispatch considering load frequency relief," *IEEE Transaction on Power Systems*, vol. 35, no. 4, pp. 3065-3077, July 2020.
- [38] H. Gu, R. Yan, T. K. Saha and E. Muljadi, "System strength and inertia constrained optimal generator dispatch under high renewable penetration," *IEEE Trans. Sustainable Energy*, vol. 11, no. 4, pp. 2392-2406, Oct. 2020.
- [39] IEEE/CIGRE: "FACTS overview", IEEE Special Issue, Piscataway, NJ, USA, 1995.
- [40] "IEEE Xplore Book Abstract - Understanding FACTS: concepts and technology of flexible AC transmission systems." [Online]. Available: <https://ieeexplore.ieee.org/book/5264253>. [Accessed: 28-June-2020].
- [41] Le, V., Li, X. and Le, C., "A novel method for seeking optimal placement of TCSC to damp oscillations in power systems", *International Journal of Control and Automation*, vol. 8, no. 4, pp.333-346, 2015.
- [42] M. Q. Tran, M.C. Dinh, S. J. Lee, J. I. Lee, M. Park, C. H. Lee and J. Yoon, "Analysis and mitigation of subsynchronous resonance in a korean power network with the first TCSC installation", *Energies*, vol. 12, no.15, pp.2847-2862, 2019.

- [43] B. Singh and R. Kumar, "A comprehensive survey on enhancement of system performances by using different types of facts controllers in power systems with static and realistic load models," *Energy Reports*, vol. 6, pp. 55–79, 2020.
- [44] D. Chatterjee, and A. Ghosh, "TCSC control design for transient stability improvement of a multi-machine power system using trajectory sensitivity", *Electric Power Systems Research*, vol. 77(5-6), pp.470-483, 2007.
- [45] M. Deepak and R. J. Abraham, "Load following in a deregulated power system with thyristor controlled series compensator," *International Journal of Electrical Power & Energy Systems*, vol. 65, pp. 136–145, 2015.
- [46] Hamsic, N., A. Schmelter, A. Mohd, E. Ortjohann, E. Schultze, A. Tuckey, and J. Zimmermann, "Increasing renewable energy penetration in isolated grids using a flywheel energy storage system", In Proc. *2007 International Conference on Power Engineering, Energy and Electrical Drives*, pp. 195-200. IEEE, 2007.
- [47] S. Muyeen, "Application of pumped storage to increase renewable energy penetration in autonomous island systems", *Wind Energy Conversion Systems*, Springer Science & Business Media, 2012.
- [48] R. R. Nejad, S. M. Hakimi, and S. M. M. Tafreshi, "Smart virtual energy storage control strategy to cope with uncertainties and increase renewable energy penetration," *Journal of Energy Storage*, vol. 6, pp. 80–94, 2016.
- [49] Saberian, A., Farzan, P., Nejad, M.F., Hizam, H., Gomes, C., Radzi, M.A.M. and Ab Kadir, M.Z.A., "Role of FACTS devices in improving penetration of renewable energy". In Proc. *2013 IEEE 7th International Power Engineering and Optimization Conference (PEOCO)* (pp. 432-437). IEEE, 2013.
- [50] Sreejith, S., Rangarajan, S. S., Ambili, M., Sujyothi, P., & Nithya, V. G., "Enhancing the power transfer capability in a power system network using series connected FACTS devices for increased renewable penetration", In Proc. *2014 International Conference on Advances in Electrical Engineering (ICAEE)* (pp. 1-6). IEEE, 2014.
- [51] Chavan, G.S., "Dynamic control of FACTS devices to enable large Scale penetration of renewable energy resources". PhD dissertation, North Carolina State University, 2017.

- [52] Li, J., Gee, A.M., Zhang, M. and Yuan, W., “Analysis of battery lifetime extension in a SMES-battery hybrid energy storage system using a novel battery lifetime model”, *Energy*, vol. 86, pp.175-185, 2015.
- [53] Ise, T., Kita, M. and Taguchi, A., “A hybrid energy storage with a SMES and secondary battery”, *IEEE Trans. Applied Superconductivity*, vol. 15, no. 2, pp.1915-1918, 2005.
- [54] Li, J., Zhang, M., Yang, Q., Zhang, Z. and Yuan, W., “SMES/battery hybrid energy storage system for electric buses”, *IEEE Trans. Applied Superconductivity*, vol. 26, no. 4, pp.1-5, 2016.
- [55] Van de Vyver, J., De Kooning, J.D., Meersman, B., Vandeveld, L. and Vandoorn, T.L., “Droop control as an alternative inertial response strategy for the synthetic inertia on wind turbines”, *IEEE Transaction on Power Systems*, vol. 31, no. 2, pp.1129-1138, 2015.
- [56] PSS[®]E User Manual, Version 34.2, Program Application Guide: Volume II, Chapter 25, pp. 25-8.
- [57] S. Eckroad, “EPRI-DOE handbook of energy storage for transmission & distribution applications”, *Electric Power Research Institute*, California, USA, pp. 349-372, 2003.
- [58] Kumar, S., Saket, R.K., Dheer, D.K., Holm-Nielsen, J. and Sanjeevikumar, P., “Reliability enhancement of electrical power system including impacts of renewable energy sources: a comprehensive review”, *IET Generation, Transmission & Distribution*, vol. 14, no. 10, pp.1799-1815, 2020.
- [59] Masood. N.A., Yan, R. and Saha, T.K., “Investigation of load frequency relief from field measurements and its impact on contingency reserve evaluation”, *IEEE Transaction on Power Systems*, vol. 33, no. 1, pp.567-577, 2017.
- [60] P. Kushwaha, V. Prakash, R. Bhakar, U. R. Yaragatti, Y. Sumanth and A. Jain, "Primary frequency response constrained energy storage scheduling under photovoltaic generation," in Proc. *2019 8th International Conference on Power Systems (ICPS)*, 2019, pp. 1-5.
- [61] M. Gibbard and D. Vowles, “Simplified 14-generator model of the SE Australian power system”, Revision 3, The University of Adelaide, South Australia, 30 June 2010.
- [62] RenewablesSA, Government of South Australia. [online]. Available: <http://www.renewablesa.sa.gov.au/topic/large-scale-generation-storage/wind-farms-south-australia> [Accessed: June 9, 2020].

- [63] PSS[®]E, “Power System Simulator for Engineering” [Online]. Available: <http://www.energy.siemens.com/hq/en/services/power-transmission-distribution/power-technologies-international/software-solutions>.
- [64] Australian Energy Market Commission, “National Electricity Rules”, version 156, chapter 5, pp. 731, 2020. Available online: <https://www.aemc.gov.au/sites/default/files/2020-12/NER%20v156%20full.pdf> [Accessed: July 2, 2021]
- [65] Australian Energy Market Commission, “Frequency Operating Standards”, 2020. Available online: <https://www.aemc.gov.au/australias-energy-market/market-legislation/electricity-guidelines-and-standards/frequency-0> [Accessed: July 2, 2021]
- [66] N.-A. Masood, M. N. H. Shazon, H. M. Ahmed, and S. R. Deebea, “Mitigation of over-frequency through optimal allocation of BESS in a low-inertia power system,” *Energies*, vol. 13, no. 17, p. 4555, Sep. 2020.
- [67] Greenwood, K. Lim, C. Patsios, P. Lyons, Y. Lim and P. Taylor, "Frequency response services designed for energy storage", *Applied Energy*, vol. 203, pp. 115-127, 2017.
- [68] National Grid. Enhanced frequency response; 2016. Available: <http://www2.nationalgrid.com/Enhanced-Frequency-Response.aspx> [Accessed: 10-Aug.-2021].
- [69] National Grid. System operability framework; 2016. Available: <https://www.nationalgrid.com/sites/default/files/documents/8589937803SOF%202016%20-%20Full%20Interactive%20Document.pdf> [Accessed: 11-Aug.-2021].
- [70] D. Jovcic and G. N. Pillai, “Analytical modeling of TCSC dynamics”, *IEEE Transaction on Power Delivery*, vol. 20, no. 2, pp. 1097-1104, 2005.
- [71] D. Mondal, A. Chakrabarti, and A. Sengupta, “Optimal placement and parameter setting of SVC and TCSC using PSO to mitigate small signal stability problem”. *International Journal of Electrical Power & Energy Systems*, vol. 42, no.1, pp.334-340, 2012.
- [72] J. Kennedy and R. Eberhart, “Particle swarm optimization”, *International Conference on Neural Networks*, Perth, WA, Australia, vol. 4, pp. 1942-1948, 1995.
- [73] Python, “pyswarm”, [Online]. Available: <https://pythonhosted.org/pyswarm/> [Accessed: 15-Jan-2020].
- [74] Siemens, “PSS[®]E User Manual”, Version 34.2, Program Application Guide: Volume II, Chapter 25, pp. 25-8.

- [75] Lee, Kwang Y., and Zita A. Vale, eds. “Applications of modern heuristic optimization methods in power and energy systems”, John Wiley & Sons, Chapter:1, pp. 2-3, 2020.
- [76] N. Masood, Yan, R. and Saha, T.K., “A new tool to estimate maximum wind power penetration level: In perspective of frequency response adequacy”. *Applied Energy*, vol. 154, pp.209-220, 2015.
- [77] G. Ben Yosef, A. Navon, O. Poliak, N. Etzion, N. Gal, J. Belikov, and Y. Levron, “Frequency stability of the Israeli power grid with high penetration of renewable sources and Energy Storage Systems,” *Energy Reports*, vol. 7, pp. 6148–6161, 2021.
- [78] Australian Energy Market Commission (AEMC), “Frequency Operation Standards”, 2020 [online]. Available: <https://www.aemc.gov.au/australias-energy-market/market-legislation/electricity-guidelines-and-standards/frequency-0> [Accessed: 24-Apr.-2022] .

Appendix A: Test System Data

Table A-1. Synchronous generator dynamic parameters

T'_{do}	T''_{do}	T'_{qo}	T''_{qo}	H	D	X_d
7.5	0.04	3.0	0.20	4.0/7.5	0	2.0
X_d	X_q	X'_d	X'_q	X''_d	X''_q	X_l
1.5	0.3	0.8	0.3	0.22	0.22	0.2

Table A-2. TCSC dynamic parameters

T_1	T_2	T_3	T_w	K
0.1	0.1	0.4	100.0	0.75
X_{MAX}	X_{MIN}	IN_{MAX}	IN_{MIN}	
0.05	0.005	1.0	0	

Table A-3. Upper and lower bounds of TCSC parameters

T_{2min}	T_{2max}	T_{3min}	T_{3max}	K_{max}	K_{min}
0.05	0.2	0.3	1.0	0.5	30

Appendix B: List of Publications

- (1) **M. N. H. Shazon**, Nahid-Al-Masood, H. M. Ahmed, S. R. Deeba and E. Hossain, "Exploring the Utilization of Energy Storage Systems for Frequency Response Adequacy of a Low Inertia Power Grid," *IEEE Access*, vol. 9, pp. 129933-129950, 2021. (Q1, Impact Factor: 3.34)
- (2) **M.N.H. Shazon**, N.A. Masood and H.M. Ahmed, "Modelling and utilisation of frequency responsive TCSC for enhancing the frequency response of a low inertia grid", *Energy Reports*, vol. 8, pp.6945-6959, 2022. (Q1, Impact Factor: 6.87)
- (3) **M.N.H. Shazon**, Nahid-Al-Masood and A. Jawad. "Frequency control challenges and potential countermeasures in future low-inertia power systems: A review", *Energy Reports*, vol. 8, pp.6191-6219, 2022. (Q1, Impact Factor: 6.87)
- (4) Nahid-Al-Masood, **M. N. H. Shazon**, H. M. Ahmed and F. Hasan, "Assessing the Risk of Blackout in a Low Inertia Power System and a Possible Countermeasure," in Proc. *2021 IEEE PES Innovative Smart Grid Technologies - Asia (ISGT Asia)*, Brisbane, Australia, pp. 1-5, 5-8 December, 2021.
- (5) **M. N. H. Shazon**, H. M. Ahmed, Nahid-Al-Masood and F. Hasan, "Supplementary Inertial Support in Renewable Integrated Networks: Potential of Synchronous Condenser and Energy Storage," in Proc. *2021 IEEE PES Innovative Smart Grid Technologies Europe (ISGT Europe)*, Espoo, Finland, 2021, pp. 1-5, 18-21 October, 2021.